A CFD Study on a Station Keeping Device for a Marine Current Turbine

Thomas Nevalainen

Master of Science in Engineering Technology
Space Engineering

Luleå University of Technology
Department of Engineering Sciences and Mathematics

LULEÅ
UNIVERSITY
OF TECHNOLOGY

In memory of my grandfather

Abstract

The last two decades have witnessed a dramatic change in nation's climate policies around the world toward a less carbon dependent energy production. This has given rise to a rapid expansion within the renewable energy sector and a wide range of alternative energy technology is in development and in use at this day. One of these upcoming technologies are the Marine Current Turbines (MCT's) which are currently undergoing extensive research and testing in the UK.

The purpose of this thesis was to investigate the performance of a novel mooring and station keeping device for a MCT in the form of a buoyant hydrofoil. The hydrofoil was designed to generate lift in the tidal stream in addition to its buoyancy and is therefore proposed to be a more efficient station keeping device than a submerged buoy.

The analysis of the hydrofoil was done by steady- state computational fluid dynamics studies where several different geometrical configurations were compared in terms of the generated mooring angle. The devices were also evaluated in construction complexity and the ratio between generated buoyancy and lift. The study was divided into two parts where the first one was a 2D study aimed at determining the most suitable foil profile for the device. The second part of the thesis was devoted to finding the approximate dimensions for the hydrofoil using a 3D analysis setup.

The findings showed that the most suitable foil shapes were the Joukowski and the NACA0025 profiles and the dimensions of the hydrofoil for a 10m diameter, 250kW turbine was 7m in chord length and 17m in width. The findings also showed that adding circular end plates to the NACA0025 geometry greatly improved its performance and gave a final mooring angle of 38.49 degrees.

The findings in this thesis should be considered as a 'proof of concept' rather than accurate data to base critical design factors on. This is due to several constraints imposed partially by the limited processing power available and the lack of data from the turbulent flow conditions in tidal streams.

A lot of research remains to be done before the concept is confidently proven to work in practice, but, according to the author, this thesis provides grounds that there is good reason to further the development of the concept.

Contents

Preface

This thesis is the part of the final project for a MSc Degree in Aerospace Engineering at the Department of Computer Science, Electrical and Space Engineering at Luleå University of Technology. The project was conducted during an international exchange at Strathclyde University and supervised by Dr Andrew Grant at the Department of Mechanical and Space Engineering. My examiner in Sweden was PhD Lars- Göran Westerberg and the thesis was presented in Luleå and a copy of the report was sent to the Strathclyde affiliated company Nautricity.

I would like to thank my supervisor Dr Grant for giving me the opportunity to conduct my thesis at Strathclyde University and for all the help and advice he has given me. I would also like to thank Dr Wendy Liu for all his invaluable help and all the PhD students at the Department of Naval Architecture. Furthermore, I want to thank the team of Sustainable Engineering students that I collaborated with for all the help and good times in Scotland.

Finally, I want to sincerely thank my mother, father and sisters for all your support and encouragement which has given me the motivation to get where I am today.

LIST OF FIGURES

List of tables

Nomenclature

Abbreviations

AoA	Angle of attack
CFD	Computational Fluid Dynamics
CPU	Central Processing Unit
CORMAT	Counter Rotating Marine Turbine
DC	Direct Current
DNS	Direct Numerical Simulation
ESRU	Energy Systems Research Unit
LES	Large Eddy Simulation
MCT	Marine Current Turbine
NACA	National Advisory Committee for Aeronautics
RANS	Reynolds Averaged Navier Stokes
SST	Shear Stress Transfer

Commonly used symbols

A	Projected area of hydrofoil
B	Buoyancy
C_D	Drag coefficient
C_L	Lift coefficient
C_P	Power coefficient
C_M	Moment coefficient
D	Drag
E	Energy output
$\bar{g}$	Gravitational acceleration
h	Operational height
k	Turbulent kinetic energy
L	Lift
M	Moment
m	Hydrofoil mass
P	Pressure
R	Turbine radius
T	Tidal period
y^+	Dimensionless wall distance
u	x- velocity component
v	y- velocity component
w	z- velocity component
Φ	Mooring angle
μ	Dynamic viscosity
τ_{ij}	Total shear stress tensor
ρ	Fluid density

1 Introduction

This chapter introduces the reader to the thesis and gives some background about the current Scottish energy policy, as well as an introduction to Marine Current Turbines (MCT's) and their possible future role as a major source of clean, renewable energy.

1.1 Background

In the past decade, governments around Europe and the world have shown increasing interest in reducing their carbon emissions.

According to the Scottish 2009 'Climate Change Delivery Plan' the Scottish government wants to place Scotland in a world leading position in clean energy usage and development [1]. The bill pledges support to the development of renewable energy technology in order for Scotland to achieve a 50% renewable electricity production by 2020. For this to be realised there must be an expansion in alternative renewable energy resources such as marine energy.

This project was done in collaboration with the department of Mechanical & Aerospace Engineering at the University of Strathclyde in Glasgow and the tidal energy developer Nautricity. The project aims to a CFD study in a pre study of using a buoyant hydrofoil as a support for a neutrally buoyant MCT called CoRMaT (Counter Rotating Marine Turbine).

1.1.1 Scottish Energy Policy

Claiming to be the most ambitious climate change legislation in the world, the Scottish Climate Change Delivery Plan poses great challenges both technical and in a social structural manner.

The main goal of the bill is to reduce Scotland's total carbon dioxide emissions by 80% at 2050 compared to the 1990's levels and having an interim goal of 34% CO2 reduction by 2020. Along with this, it is also pledged that 50% of all generated electricity shall be from a renewable source at 2020 [1].

In order to achieve the goal of 50% of national electricity production coming from renewable sources, Scotland is required to expand its renewable sector with 8.4 GW by 2020. This in turn requires large investments in the development of new forms of renewable energy generators such as offshore wind turbines and the exploitation of marine energy, such as tidal and wave energy.

The Scottish government has the ambition to encourage growth of the renewable energy sector by the means of financial levers to promote investments, which in turn would lead to large scale development. This has the potential to lead to economic growth in the form of new job opportunities and technology export as the CO2 emissions are reduced [2].

Furthermore, Scotland has an estimated 60 GW of raw renewable electricity resources which, with the right technology development, could lead to a significant green electricity export to the UK and beyond [1].

1.1.2 MCT's and their Potentials

Marine current turbines are powered mainly by high velocity tides created when the moon's gravitational field forces water through narrow passes of land masses. Due to the variations of tidal ranges and land mass configurations around the world, the potential sites where installations of MCT's would be economically defendable are not many. But in the sites where high velocity tidal streams do exist they could be a much needed addition to the renewable electricity generation mix, due to some unique advantages discussed below. Figure 1 shows the areas around the world with the most promising tidal resources exploitable for a reasonable price, expressed in GW [7].
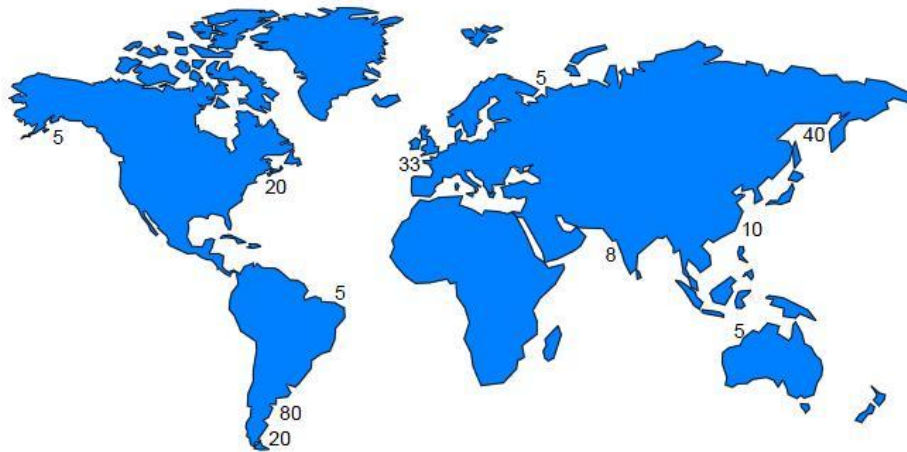
Figure 1: World map showing exploitable tidal resources in GW.

The estimated global tidal turbine energy potential is said to be 120 GW and in the UK alone it has an estimated 10 GW potential, which equates to 15% of the total UK electricity demand. The energy produced by MCT's could power 15 million homes in the UK and save 70 million tonnes of CO_2 and in the same time create 16000 new jobs [2].

One unique advantage that MCT's have in front of other renewable electricity generators, such as wind power turbines, is their inherit predictability due to predictable tides. Solar, wind and wave power generators generally require backup from conventional fossil fuels sources to compensate downtime at low wind and sun conditions. Wind and wave turbines also have to be engineered to withstand extreme conditions during storms and baffling winds which increase their costs and complexities. The fact that the energy output of a MCT can be very accurately predicted makes them highly attractive for grid management and allows them to be engineered for exact operating conditions.

Another obvious advantage is that due to the high density of water MCT's can be made much more compact than their wind driven counterparts for the same energy production. This allows for higher packing density in array configurations which is of economical and environmental importance [2].

The technology of MCT's is still immature and only a few commercial large scale turbines exist around the world, notably the 1.2 MW SeaGen turbine in the Strangford Narrows (figure 2) [3].
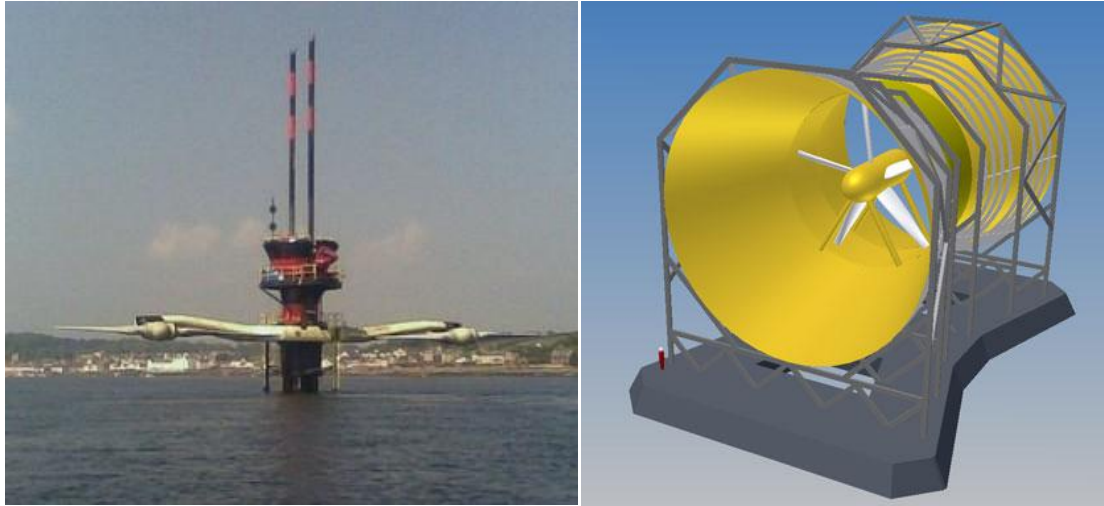
Figure 2: Left, The 1.2 MW double generator SeaGen can be raised above water for maintenance. Right, the Lunar Energy's RTT ducted turbine.

There exists many different proposed designs of MCT's and their mooring methods where the main types are horizontal axis turbines, vertical axis turbines and oscillating hydrofoils. Although there is no clear design superiority yet in MCT's as in wind turbines, the horizontal axis model is the most proposed solution so far. The right hand side of figure 2 shows a MCT developed by Lunar Energy that has a ducted vent and sits on the seabed using a gravity base.

In the large scale production and installation of commercial MCT's the industry may draw upon knowledge from the oil and gas industry for material choices, corrosion protection and maintenance as well as using methods developed in the wind turbine industry for blade design and performance calculations. Many currently deployed MCT's have adopted conventional two or three blade configurations from wind turbine practice and although the fluid dynamics of MTC's are similar to those in wind turbines, there several differences in the flow characteristics given by the upper and lower boundary constraints and differences in turbulence [9].

There exists a wide range of proposed solutions for the mooring of MCT's ranging from rigid piles and gravity bases to floating platforms and tensioned flexible arrangements [4]. Gravity bases and rigid piles have the disadvantage of being expensive and not deployable at great depth, the advantage however is that the wealthy oil and gas industry is experienced in marine structures. Tether moorings from floating platforms and flexible mooring points are a cheaper alternative with the advantage of being deployable on greater depths than gravity bases and allow the turbines to naturally align themselves in the alternating tides. The disadvantages are possible stability issues related to free floating objects in a tidal stream.

Finally there are several environmental impacts that must be considered when considering using MCT's on a large scale. Although believed to be of small scale, the main issue raised is the possibility of their impact on flow and sediment transfer during and after installation. There is also a concern of damaging marine life through rotor collision, but since the rotor speed of an MCT is very low compared to a wind turbine or propeller, this is considered unlikely [5]. Another issue that must be

considered is that the turbines do not interfere with other users of the sea such as shipping or fishing.

1.1.3 Nautricity

Nautricity is a renewable technology company specialising in MCT's and was founded as a spin-off company from Strathclyde Universities Energy Systems Research Unit (ESRU). The company's foundation was realised after an investment deal was forged with the privately owned company First Tech. Nautricity has a team of 4 employees and is based in central Glasgow and their main achievement is the further development and deployment of the ESRU developed MCT CoRMaT. The technology used by Nautricity has been developed and supported by Strathclyde University and although being a young company, the Nautricity team is already in discussion with a number of international organisations looking to deploy its patented MCT [6]. The team was also awarded with the prestigious Technology Award at the Energy Institute Awards in November 2010.

1.1.4 CoRMaT

The CoRMaT was developed by ESRU at Strathclyde University and is designed to extract tidal energy from a wide range of water depths by "flying" a neutrally buoyant device from a flexible tensioned mooring [8].

The turbine has two counter rotating, dissimilar rotors in close proximity (figure 3) to minimise the reactive torque on the support structure and minimise the swirl in the turbulent wake. This allows for a simple and economical mooring system to be utilised in the form of a flexible tether which can be deployed in deep water and allows the turbine to align itself in the alternating tides.
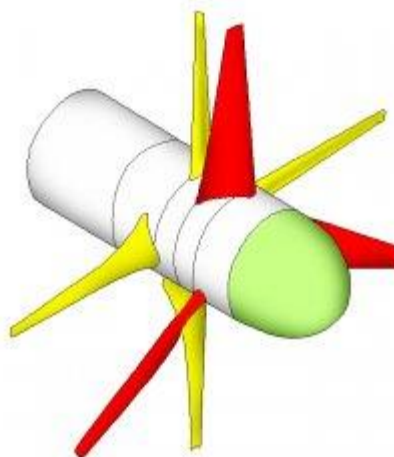
Figure 3: 3D rendering of the CoRMaT turbine

The benefit of swirl reduction in the turbines wake due to the counter rotating blades has the possible advantage of allowing the turbines to be placed closer together in an array formation. Increasing the array packing density will allow for better energy exploitation of coastal areas. The reduced wake swirl may also reduce the scouring of the seabed which will leave the local ecosystem less affected [9]. The fluid dynamics of a counter rotating MCT is highly complex and stretches the boundaries of computational methods, therefore more quantitative studies must be performed on this area before any definite conclusions can be drawn.

Figure 4: The 2.5m diameter prototype being lowered into the river Clyde for testing.

A 2.5m diameter prototype of the CoRMaT has been constructed and has undergone testing in the river Clyde estuary (figure 4). The test proved the designs inherent stability given by the structures drag. Another question to be answered was the blade loadings caused by the blade- blade interactions. These loadings were thought to give rise to fatigue damage over long time but the study showed that these forces were small compared to the gravitational loading of the structure and thus negligible. The next step in the production process is to construct a 10m diameter turbine which this thesis uses for reference values.

The generator used in the CoRMaT turbine is a direct drive generator thus the large nacelle diameter. Due to the slow rotational speed of MCT's, heavy and expensive gearboxes are needed if they are to be fitted with common 4- pole generators. Direct drive generators with a large number of poles is therefore more beneficial [8]. The generator is fully submersible, meaning that both the rotors and stators operate in sea water and produce a 3-phase output converted to DC which allows for efficient transmission under water. The DC is then inverted at the end of the grid. The advantages of having a submersible generator are ease of construction, no leakage issues, natural cooling and no complex sealing. The rotors and permanent magnets are covered in polymer resin to prevent corrosion.

The flexible tether mooring used on CoRMaT has several great advantages as compared conventional rigid moorings but also pose some problems that must be dealt with. One problem is for the mooring to keep the turbine in a reasonable span of operational depth, that is, not allowing the turbine to move up and down too much under changing tide velocities. As a mean to counter this phenomenon, the addition of an auxiliary float above the neutrally buoyant turbine has been suggested as shown in figure 5.
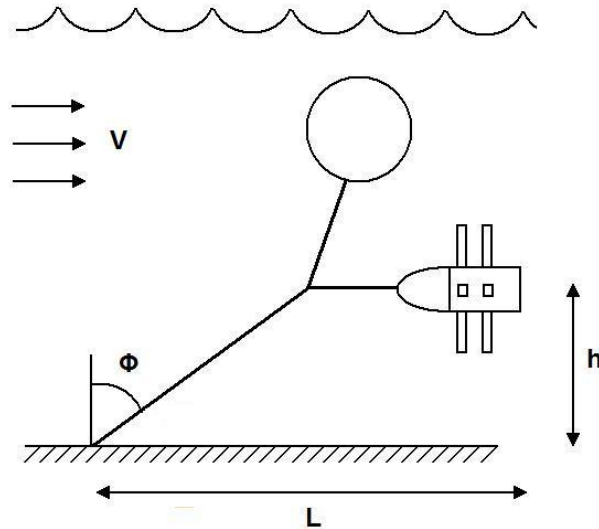
Figure 5: Schematic drawing of the turbine buoy configuration where h is the operating height, L is the footprint length and phi is the mooring angle.

The purpose of adding this extra buoyancy was to reduce the angle Φ which allows for grater turbine packing density and minimises the variation in operational depth h. A drawback when using a conventional buoy to add extra buoyancy to the turbine is that the buoy has high drag and no lift force and if it were to be placed on the surface to reduce the drag, it could become an obstacle for shipping of fishing vessels. Other problems faced when using flexible moorings was the risk of the turbine tangling in slack water. Suggested measures to counter this included the addition of thrusters on the turbine to provide stability.

A suggested alternative to reduce the mooring angle Φ other than using a buoy was to use a buoyant hydrofoil or "underwater wing". This configuration had the advantage of adding buoyancy and lift to the turbine and providing less drag than a submerged buoy. The purpose of this project was to investigate how much the mooring angle Φ could be reduced with the use of a buoyant hydrofoil.

1.2 Purpose of the Project

The purpose of the project was to conduct an investigation on how much the angle of the 10m diameter turbine and float configuration to the sea bed Φ could be reduced by the use of a buoyant hydrofoil. The study was to be conducted using a commercially available CFD package and the results of the angle Φ were to be presented to an engineer at Nautricity for evaluation of it feasibility.

With the mooring angle Φ known one could make an estimation on the packing density of the turbines and give a rough evaluation on a turbine arrays site efficiency, thereby giving an approximation of the price of the produced electricity.

1.3 Limitations

A number of limitations had to be set on the study due to the lack of time and computing power available. All CFD simulations done were steady state as to save computing time and the surface boundary mesh resolution was not set very high in the 3D case (as described in section 3.3) due to lack of processing power. This posed some limitations in the accuracy of the results but they were not considered to be of great importance since the study was of a "proof of concept" nature.

Furthermore, the surface boundary flow conditions were assumed to not have a great impact in the flow characteristics of the problem.

Another limitation was that since only steady state analysis was performed, the performance of the hydrofoil in all flow velocities was not examined. Only the maximum stream velocity of 3 m/s was investigated. The steady state analysis also gives no information about the hydrodynamic stability of the geometry.

The modelling of the turbulent conditions of a tidal current was also limited by the fact that there exists very little data on the subject available to the public. Instead, an approximation of the turbulent intensity and the eddy length scale was used. Furthermore, the turbine was assumed to operate at a depth were surface and wave interactions were negligible to greatly simplify the simulation complexity.

1.4 Problem Description

1.4.1 Choosing a suitable hydrofoil profile

Since the hydrofoil was intended to be a hybrid between a floatation device and a lift generating device a thick profile was needed. Due to the sparseness of experimental data on thick hydrofoils and the unusual operating conditions presented in a tidal stream, a study had to be conducted to determine which profile was best suited for the task. This was done by comparing several different thick hydrofoil and airfoil profiles using 2D CFD analysis and determining what their angles of attack (AoA) were at the maximum lift to drag ratio.

1.4.2 Determining the dimensions of the hydrofoil

With a suitable hydrofoil profile chosen, the dimensions of the device needed to be determined to conclude if the hydrofoil lift device was a plausible solution to the problem. With the geometry known a 3D CFD study was to be conducted to give a more accurate description of the problem. The lift and drag given from the 3D study and the geometries buoyancy were then taken into consideration to determine the mooring angle Φ and thus identifying the geometry giving the smallest footprint area.

As an effort to reduce the drag and increase the lift of the hydrofoil, several drag reducing and lift increasing features were added to the geometry and studied in 3D CFD simulations.

1.4.3 Buoy vs. Hydrofoil

During the course of the project collaborations were made with a team of students studying Sustainable Engineering at Strathclyde University [10]. The team were investigating the performance of the same tethered mooring system for the CoRMaT turbine but using a buoy instead of a hydrofoil. The results of their investigation were to be compared to the hydrofoil investigation to present the benefits and drawbacks of the two solutions and possibly present which of the two solutions was most reasonable in terms of footprint area reduction, cost and complexity.

2 Theory

In this chapter the reader is briefly introduced to the theoretical concepts involved in the project. The chapter covers the basics of Computational Fluid Dynamics as well as the definitions of the forces acting on the hydrofoil together with the fundamental equation for MCT energy capture. This

is followed by an overview of the high lift and low drag devices examined and finally some information on the velocity profiles in tidal currents.

2.1 Computational Fluid Dynamics

Computational Fluid Dynamics (CFD) is a discipline in the field of fluid mechanics which uses numerical methods and algorithms to solve complex problems involving fluid flow. CFD is used in a wide range of industrial and scientific applications from internal combustion engines to cardiovascular flow to determine parameters such as fluid velocity, pressure, temperature, density and much more.

The basic concept is to use computers to iteratively solve the governing non- linear equations. These equations can be derived by applying Newton's 2nd law of conservation of momentum to an arbitrary volume of the fluid continuum.

For an incompressible isothermal fluid the governing equation for conservation of momentum is

$$\rho\left(\frac{D\bar{V}}{Dt}\right) = -\bar{\nabla}P + \rho\bar{g} + \mu\nabla^2\bar{V}$$

(2.1)

where ρ is the fluid density, $\bar{V}$ is the velocity field vector, P is the pressure, $\bar{g}$ is the gravitational acceleration and μ is the dynamic viscosity. Equation 2.1 is called the Navier- Stokes equation after its discoverers and it relates the fluid velocity to the density and pressure, more information of the Navier- Stokes equation and its derivation can be found in 'Fluid mechanics fundamentals and applications' by Y.A Cengel and J.M Cimbala.

Expanded in Cartesian coordinates (x, y, z) and (u, v, w) equation (2.1) becomes

x- component

$$\rho\left(\frac{\partial u}{\partial t} + u\frac{\partial u}{\partial x} + v\frac{\partial u}{\partial y} + w\frac{\partial u}{\partial z}\right) = -\frac{\partial P}{\partial x} + \rho g_x + \mu\left(\frac{\partial^2 u}{\partial x^2} + \frac{\partial^2 u}{\partial y^2} + \frac{\partial^2 u}{\partial z^2}\right)$$

(2.2)

y- component

$$\rho\left(\frac{\partial v}{\partial t} + u\frac{\partial v}{\partial x} + v\frac{\partial v}{\partial y} + w\frac{\partial v}{\partial z}\right) = -\frac{\partial P}{\partial y} + \rho g_y + \mu\left(\frac{\partial^2 v}{\partial x^2} + \frac{\partial^2 v}{\partial y^2} + \frac{\partial^2 v}{\partial z^2}\right)$$

(2.3)

z- component

$$\rho\left(\frac{\partial w}{\partial t} + u\frac{\partial w}{\partial x} + v\frac{\partial w}{\partial y} + w\frac{\partial w}{\partial z}\right) = -\frac{\partial P}{\partial z} + \rho g_z + \mu\left(\frac{\partial^2 w}{\partial x^2} + \frac{\partial^2 w}{\partial y^2} + \frac{\partial^2 w}{\partial z^2}\right)$$

(2.4)

and expanded in Cartesian coordinates the continuity equation that determines the conservation of mass flow becomes

$$\frac{\partial u}{\partial x} + \frac{\partial v}{\partial y} + \frac{\partial w}{\partial z} = 0.$$

(2.5)

Due to the non- linearity of the governing partial differential equations above it is not possible to get an exact analytical solution of them but for the simplest of cases. For this reason it is necessary to discretise the problem commonly by dividing the flow domain in to computational points where the physical properties are evaluated and also discretizing equations (2.2) to (2.5).

In the CFD solver FLUENT used in this project equations (2.2) to (2.5) discretised in to a set of linear algebraic equations and integrated over the small volumes surrounding each computational point called nodal points [11]. This solution method is called the finite- volume method and it has the advantage of being easily formulated to cope with unstructured nodal meshes.

2.1.1 Turbulence

When modelling turbulent flows in CFD one is confronted with several difficulties that are not present in laminar flow. The problem is that turbulent flows contain many random and chaotic rotational flow patterns called eddies that have a wide range of velocity, pressure and length scales.

Due to this complex behaviour the modelling of turbulence is in many cases computationally expensive. For this reason most CFD calculations are done with turbulence models that calculate the properties of differing eddy length scales on a statistical basis. The most common techniques are the DNS, LES and RANS methods presented below. The DNS and LES methods are not used in this thesis and will only be given a brief introduction.

The Direct Numerical Simulation (DNS) technique resolves the entire range of turbulent eddy length scales. This greatly reduces the errors inherent with statistical models but is so calculation expensive that is not a feasible method for more complex flow situations [12].

Large Eddy Simulation (LES) significantly less computationally intense than the DNS method due to its use of statistical models. In this model the smallest eddies are replaced with models and the large and more important eddies resolved. This model is however not as computationally efficient as the RANS described below.

2.1.1.1 Reynolds Averaged Navier- Stokes Equation

The Reynolds Averaged Navier- Stokes Equation (RANS) is the turbulence equation used in this thesis due to the CPU effectiveness and robustness that this method brings. In this method none of the turbulent eddies are resolved but instead replaces the Navier- Stokes and continuity equation with the Reynolds Averaged Navier- Stokes Equation. This new governing equation however presents new unknowns namely the Reynolds stresses which must be approximated by the use of a turbulence model. The derivation of the RANS is as follows, as according to [13]:

Transforming the Navier- Stokes Equation into the RANS is based on an assumption called Navier- Stokes decomposition which states that the time dependant chaotic fluctuations of the turbulent flow can be separated from the mean flow parameters as illustrated in figure 6.
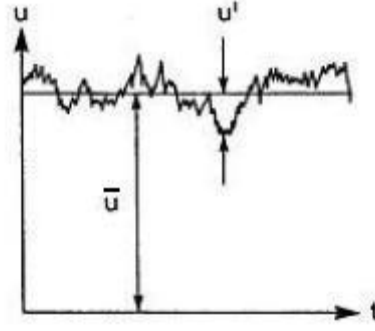
Figure 6: The flow momentary velocity component u is composed by the fluctuating velocity u' and the average velocity $\bar{u}$.

The mathematical relationship between the momentary velocity component u, the time averaged velocity component $\bar{u}$ and the time dependent fluctuating velocity component u' can be written as

$$u = \bar{u} + u'.$$

(2.6)

This relationship holds true for all velocity components (u, v, w) as well as for the pressure, density and temperature, although the temperature and pressure are considered constant in this case.

$$v = \bar{v} + v',$$

$$w = \bar{w} + w',$$

$$p = \bar{p} + p',$$

$$\rho = \bar{\rho} + \rho',$$

$$T = \bar{T} + T'$$

One method of averaging the parameters is to take the mean values at a fixed place in space and using a time span large enough for the mean values to be independent of it as in equation (2.7).

$$\bar{u} = \frac{1}{\Delta t} \int_{t_0}^{t_0+t_1} u \, dt$$

(2.7)

The time averaged values of the fluctuating components are defined to be zero:

$$\overline{u'} = 0, \quad \overline{v'} = 0, \quad \overline{w'} = 0, \quad \overline{p'} = 0.$$

(2.8)

Firstly the continuity equation is decomposed and averaged. Combining the relation (2.6) for all the velocity components with the continuity equation we get:

$$\frac{\partial \bar{u}}{\partial x} + \frac{\partial u'}{\partial x} + \frac{\partial \bar{v}}{\partial y} + \frac{\partial v'}{\partial y} + \frac{\partial \bar{w}}{\partial z} + \frac{\partial w'}{\partial z} = 0.$$

$$(2.9)$$

The time- averaging of equation (2.9) is written as:

$$\frac{\overline{\partial \bar{u}}}{\partial x} + \frac{\overline{\partial u'}}{\partial x} + \frac{\overline{\partial \bar{v}}}{\partial y} + \frac{\overline{\partial v'}}{\partial y} + \frac{\overline{\partial \bar{w}}}{\partial z} + \frac{\overline{\partial w'}}{\partial z} = 0.$$

$$(2.10)$$

A summary of the rules for time- averaging is presented here for the clarification of the following transformations:

$$\frac{\overline{\partial \bar{u}}}{\partial x} = \frac{1}{\Delta t} \int_{t_0}^{t_0+t_1} \frac{\partial u}{\partial x} dt = \frac{\partial}{\partial x} \frac{1}{\Delta t} \int_{t_0}^{t_0+t_1} u \, dt = \frac{\partial \bar{u}}{\partial x}$$

$$(2.11)$$

$$\frac{\overline{\partial u'}}{\partial x} = \frac{1}{\Delta t} \int_{t_0}^{t_0+t_1} \frac{\partial u'}{\partial x} dt = \frac{\partial}{\partial x} \frac{1}{\Delta t} \int_{t_0}^{t_0+t_1} u' \, dt = 0$$

$$(2.12)$$

$$\bar{\bar{f}} = \bar{f}, \qquad \overline{f+g} = \bar{f} + \bar{g}, \qquad \overline{\bar{f} \cdot g} = \bar{f} \cdot \bar{g}, \qquad \frac{\overline{\partial f}}{\partial s} = \frac{\partial \bar{f}}{\partial s}, \qquad \overline{\int f \, ds} = \int \bar{f} ds$$

But $\overline{f \cdot g} \neq \bar{f} \cdot \bar{g}$.

$$(2.13)$$

The averaged derivatives of the fluctuations are also zero according to these rules which simplifies equation (2.10) to the averaged continuity equation

$$\frac{\partial \bar{u}}{\partial x} + \frac{\partial \bar{v}}{\partial y} + \frac{\partial \bar{w}}{\partial z} = 0.$$

$$(2.14)$$

The averaging of the Navier- Stokes equation will be shown using the x- component of the velocity (Equation 2.2) but before that a small transformation will be done to the advection term of it:

$$u\frac{\partial u}{\partial x} + v\frac{\partial u}{\partial y} + w\frac{\partial u}{\partial z} = \frac{\partial (u^2)}{\partial x} + \frac{\partial (uv)}{\partial y} + \frac{\partial (uw)}{\partial z} - u\left(\frac{\partial u}{\partial x} + \frac{\partial v}{\partial y} + \frac{\partial w}{\partial z}\right) = \frac{\partial (u^2)}{\partial x} + \frac{\partial (uv)}{\partial y} + \frac{\partial (uw)}{\partial z}$$

$$(2.15)$$

11

The expressions for the decomposed components (Equations 2.6 and below) and equation (2.15) are now substituted into Equation (2.2) and time averaged:

$$\overline{\rho\left\{\frac{\partial(\bar{u}+u')}{\partial t}+\frac{\partial(\bar{u}+u')^2}{\partial x}+\frac{\partial(\bar{u}+u')(\bar{v}+v')}{\partial y}+\frac{\partial(\bar{u}+u')(\bar{w}+w')}{\partial z}\right\}}$$
$$=F_x-\frac{\partial(\bar{p}+p')}{\partial x}+\mu\overline{\left\{\frac{\partial^2(\bar{u}+u')}{\partial x^2}+\frac{\partial^2(\bar{u}+u')}{\partial y^2}+\frac{\partial^2(\bar{u}+u')}{\partial z^2}\right\}}.$$

(2.16)

Applying the rules from (2.11) to (2.13) reduces equation (2.16) to

$$\rho\left(\frac{\partial\bar{u}}{\partial t}+\frac{\partial\overline{uu}}{\partial x}+\frac{\partial\overline{u'u'}}{\partial x}+\frac{\partial\overline{uv}}{\partial y}+\frac{\partial\overline{u'v'}}{\partial y}+\frac{\partial\overline{u'w'}}{\partial z}+\frac{\partial\overline{uw}}{\partial z}\right)=F_x-\frac{\partial\bar{p}}{\partial x}+\mu\left(\frac{\partial^2\bar{u}}{\partial x^2}+\frac{\partial^2\bar{u}}{\partial y^2}+\frac{\partial^2\bar{u}}{\partial z^2}\right).$$

(2.17)

Further simplifications of equation (2.17) such as repeated application of the product rule and using the continuity equation on the advection term lead to a form of the RANS for all directions as:

x- component

$$\rho\left(\frac{\partial\bar{u}}{\partial t}+\bar{u}\frac{\partial\bar{u}}{\partial x}+\bar{v}\frac{\partial\bar{u}}{\partial y}+\bar{w}\frac{\partial\bar{u}}{\partial z}\right)=F_x-\frac{\partial\bar{p}}{\partial x}+\mu\Delta\bar{u}-\rho\left(\frac{\partial\overline{u'u'}}{\partial x}+\frac{\partial\overline{u'v'}}{\partial y}+\frac{\partial\overline{u'w'}}{\partial z}\right)$$

y- component

$$\rho\left(\frac{\partial\bar{v}}{\partial t}+\bar{u}\frac{\partial\bar{v}}{\partial x}+\bar{v}\frac{\partial\bar{v}}{\partial y}+\bar{w}\frac{\partial\bar{v}}{\partial z}\right)=F_y-\frac{\partial\bar{p}}{\partial y}+\mu\Delta\bar{v}-\rho\left(\frac{\partial\overline{u'v'}}{\partial x}+\frac{\partial\overline{v'v'}}{\partial y}+\frac{\partial\overline{v'w'}}{\partial z}\right)$$

z- component

$$\rho\left(\frac{\partial\bar{w}}{\partial t}+\bar{u}\frac{\partial\bar{w}}{\partial x}+\bar{v}\frac{\partial\bar{w}}{\partial y}+\bar{w}\frac{\partial\bar{w}}{\partial z}\right)=F_z-\frac{\partial\bar{p}}{\partial z}+\mu\Delta\bar{w}-\rho\left(\frac{\partial\overline{u'w'}}{\partial x}+\frac{\partial\overline{v'w'}}{\partial y}+\frac{\partial\overline{w'w'}}{\partial z}\right)$$

(2.18)

and in tensor form:

$$\rho\frac{D\bar{u}_i}{Dt}=F_i-\frac{\partial\bar{p}}{\partial x_i}+\mu\Delta\bar{u}_i-\rho\underbrace{\left(\frac{\partial\overline{u'_iu'_j}}{\partial x_j}\right)}_{Reynolds\ Stress}.$$

(2.19)

Here on forth the time-averaged fields will not be over-lined anymore. As an example u stands for the time- averaged velocity component in the x- direction.

Looking at the last two terms on the right hand side of equation (2.19) it is possible to make a rearrangement to make clearer what the time averaging has added to the Navier- Stokes equation:

$$\mu \Delta u_i - \rho \left(\frac{\partial \overline{u'_i u'_j}}{\partial x_j} \right) = \mu \frac{\partial}{\partial x_j} \left(\frac{\partial u_i}{\partial x_j} \right) - \rho \frac{\partial}{\partial x_j} \left(\overline{u'_i u'_j} \right) = \frac{\partial}{\partial x_j} \left(\mu \frac{\partial u_i}{\partial x_j} - \rho \overline{u'_i u'_j} \right).$$

(2.20)

The expression in the brackets at the far right side of equation (2.20) corresponds to the total shear stress:

$$\tau_{ij} = \mu \frac{\partial u_i}{\partial x_j} - \rho \overline{u'_i u'_j}$$

(2.21)

where τ_{ij} is the total shear stress tensor composed of the molecular stress tensor as the first term on the right hand side of equation (2.21) and the Reynolds stress tensor as the second term. The Reynolds stress tensor arises from the time- averaging process and adds a new set of unknowns to the equation. To model these stresses in order to close the RANS equation it is possible to use eddy viscosity principle derived by Boussinesq in 1877 (also called Boussinesq hypothesis). In this principle the RANS equation can be written on the form

$$\rho \left(\frac{Du_i}{Dt} \right) = F_i - \frac{\partial p}{\partial x_i} + \frac{\partial}{\partial x_j} \tau_{ij}$$

where the total shear stress tensor is

$$\tau_{ij} = \mu \frac{\partial u_i}{\partial x_j} + \rho \left(v_t \left(\frac{\partial u_i}{\partial x_j} + \frac{\partial u_j}{\partial x_i} \right) - \frac{2}{3} k \delta_{ij} \right)$$

(2.22)

and v_t is the eddy viscosity, δ_{ij} is the Kronecker delta and k is the turbulent kinetic energy. In this principle the problem of finding the Reynolds stresses are replaced by the task of finding a model for the eddy viscosity, so called turbulence models. The turbulence models considered for this thesis are presented in the next section.

2.1.1.2 Turbulence models

RANS- based turbulence models ultimately compute the Reynolds stresses in order to have a even number of equations and unknowns which closes the RANS equation. The RANS based turbulence models can be divided in to three families of increasing complexity. These are the Linear Eddy Viscosity Models, the Non-linear Eddy Viscosity Models, and the Reynolds Stress Models. The Linear Eddy Viscosity Models have more or less become industry standard because of their effectiveness and reliability and for this reason, only turbulence models in this family have been considered for this thesis.

The Linear Eddy Viscosity models are all based on the Boussinesq hypothesis shown in equation (2.22) and can be further broken down in to three sub- classes. These are the algebraic models, the

one equation models and the two equation models. Here follows an overview of the turbulence model sub- classes.

Unlike the one and two equation models, the algebraic models (zero equation models) do not require the solution of an additional set of equations. Instead, the Reynolds stresses are approximated directly from the flow variables. This approach is often too simple for use in general purposes since they do not account for history effects on the turbulence.

One equation models solve one turbulent transport equation as the name suggests, usually the turbulent kinetic energy equation. The most famous model in this sub- class is the Spalart- Allmans model.

The most commonly used turbulence models in the industry are the two equation models that include two extra transport equations to represent the turbulent properties of the flow. This allows the models to include the history effects such as convection and diffusion of turbulent energy. In most cases one of the transported variables is the turbulent kinetic energy (k) and the second one varies depending on the model. The first variable determines the energy in the turbulence and the second one determines its scale. The most widely used transported variables are the turbulent dissipation (ε) or the specific dissipation rate (ω). The latter one is used in the k- ω models which were the turbulence models used in this project and some information about them is listed below.

2.1.1.2.1   Standard k- ω model

The k- ω model used in FLUENT 6.3 is based on the Wilcox k- ω model which is a empirical two equation model where one equation solves the turbulent kinetic energy (k) and the other the turbulent dissipation rate (ω) which can be seen as the ratio of ε and k. This approach allows for a accurate "near wall treatment" through a automatic switch between a wall function near the wall boundaries to a low Reynolds number formulation in the free stream based on the grid spacing. The model uses the gradient diffusion hypothesis to relate the Reynolds stresses to the mean velocity gradient and the turbulent viscosity.

The k- ω model displays superior performance for wall bounded boundary layers and is suited for external aerodynamics and turbo machinery analysis.

The transported variables k and ω are obtained from the following relationships:

k- transport equation

$$\frac{\partial}{\partial t}(\rho k) + \frac{\partial}{\partial x_i}(\rho k u_i) = \frac{\partial}{\partial x_j}\left(\Gamma_k \frac{\partial k}{\partial x_j}\right) + G_k - Y_k + S_k$$

(2.23)

ω- transport equation

$$\frac{\partial}{\partial t}(\rho \omega) + \frac{\partial}{\partial x_i}(\rho \omega u_i) = \frac{\partial}{\partial x_j}\left(\Gamma_\omega \frac{\partial \omega}{\partial x_j}\right) + G_\omega - Y_\omega + S_\omega.$$

(2.24)

In equations (2.23) and (2.24) G_k represents the generation of turbulent kinetic energy due to mean velocity gradients and G_ω represents the production of ω. Γ_k and Γ_ω represent the effective diffusivity of k and ω respectively and Y_k and Y_ω represent the dissipation of k and ω due to turbulence [14]. More information on the calculation of these terms can be found in the *FLUENT 6.3 Manual, chapter 12 Modelling Turbulence*. S_k and S_ω are used defined turbulence source terms.

2.1.1.2.2   SST k- ω model

The Shear Stress Transport k- ω turbulence (SST k- ω) model was developed to effectively blend the accuracy of the k- ω model near wall regions with the free stream independence of the popular k- ε in the far stream field. The transport equations of the SST k- ω model are similar to those of the standard k- ω model but have among other features a blending function that smoothly transforms the functions from a k- ω scheme near walls to a k- ε scheme in the far field. Also the definition of the turbulent viscosity is modified to account for the transport of tur bulent shear stress.

These modifications make the SST k- ω model more accurate for a wider class of flows as opposed to the standard k- ω model. These include flows with adverse pressure gradients, airfoils and transonic shock waves. The transport equations are given below:

k- transport equation

$$\frac{\partial}{\partial t}(\rho k) + \frac{\partial}{\partial x_i}(\rho k u_i) = \frac{\partial}{\partial x_j}\left(\Gamma_k \frac{\partial k}{\partial x_j}\right) + \overline{G_k} - Y_k + S_k$$

(2.25)

ω- transport equation

$$\frac{\partial}{\partial t}(\rho \omega) + \frac{\partial}{\partial x_i}(\rho \omega u_i) = \frac{\partial}{\partial x_j}\left(\Gamma_\omega \frac{\partial \omega}{\partial x_j}\right) + G_\omega - Y_\omega + D_\omega + S_\omega.$$

(2.26)

The terms in equations (2.25) and (2.26) essentially represent the same variables as in equations (2.23) and (2.24) but derived differently. Detailed information on these derivations can be found in the *FLUENT 6.3 Manual section 12.5.1 Modelling the turbulence production*. The term D_ω is however a unique function for the SST k- ω model and represents the cross diffusion blending function that is introduced when the k- ε model is transformed into equations based on k and ω. The cross diffusion blending function is defined as:

$$D_\omega = 2(1 - F_1)\rho\sigma_{\omega,2}\frac{1}{\omega}\frac{\partial k}{\partial x_j}\frac{\partial \omega}{\partial x_j}$$

(2.27)

where F_1 is a blending function and $\sigma_{\omega,2}$ is a model constant.

2.1.1.2.3   Transition SST k- ω model

The Transition SST k- ω is based on the SST k- ω model but has two extra transport equations where one calculates the intermittency and the other calculates the transition onset criteria in terms of transition momentum thickness Reynolds number. The intermittency is the probability that a certain point in the flow domain lies in the turbulent flow area.

This turbulence model is good at predicting transition from laminar to turbulent boundary layers in fully turbulent flow cases although it relies heavily on empirical correlations and constants to produce accurate results. The transport equation for the intermittency γ is defined as:

$$\frac{\partial(\rho\gamma)}{\partial t} + \frac{\partial(\rho U_j\gamma)}{\partial x_j} = P_{\gamma 1} - E_{\gamma 1} + P_{\gamma 2} - E_{\gamma 2} + \frac{\partial}{\partial x_j}\left[\left(\mu + \frac{\mu_t}{\sigma_\gamma}\right)\frac{\partial\gamma}{\partial x_j}\right]$$

(2.28)

where $P_{\gamma 1}$ and $E_{\gamma 1}$ are transition sources defined by empirical correlations that control the length of the transition region. $P_{\gamma 2}$ and $E_{\gamma 2}$ are the destruction and relaminarisation sources that are defined by empirical constants and the vorticity magnitude.

The transport equation for the transition momentum thickness Reynolds number $\widetilde{Re_{\theta t}}$ is:

$$\frac{\partial(\rho\widetilde{Re_{\theta t}})}{\partial t} + \frac{\partial(\rho U_j\widetilde{Re_{\theta t}})}{\partial x_j} = P_{\theta t} + \frac{\partial}{\partial x_j}\left[\sigma_{\theta t}(\mu + \mu_t)\frac{\partial\widetilde{Re_{\theta t}}}{\partial x_j}\right].$$

(2.29)

The detailed definition of all the unexplained variables and term definitions can be found in the Fluent 12 user manual section *4.7.2 Transport Equations for the Transition SST Model*.

2.1.1.2.4   y+

The y^+ value is a dimensionless distance from the wall to the nearest node in the computational grid in a wall bounded flow. It is defined as

$$y^+ = \frac{u_* y}{\nu}$$

(2.30)

where y is the distance between the wall and the nearest node, ν is the local kinematic viscosity and u_* is the friction velocity defined as:

$$u_* = \sqrt{\frac{\tau_w}{\rho}}$$

(2.31)

where τ_w is the wall shear stress and ρ is the fluid density at the wall.

The boundary layer of a wall bounded flow is divided into an inner and an outer region where the inner region is divided further into a laminar viscous sub layer and fully a turbulent region. In the

inner region the turbulence models employ the so called wall equations and in the fully turbulent part of the inner region the so called logarithmic laws are used. Most CFD codes assume that the viscous sub layer is located between the wall and the first node where the code switches from wall equation to log- law.

The y^+ value acts as a ratio between the turbulent and laminar flow influences in a cell and gives an indication if a cell is turbulent or laminar. This makes it possible to use the y^+ value for prediction if the turbulence models assumption of applying a viscous sub layer in the first cell is accurate. If the y^+ value is too small the second cell from the wall could have some laminar flow in it but the wall functions are not applied to it thus decreasing the models accuracy. If on the other hand the y^+ value is too big the laminar/ turbulent aspect is not that bad but other assumptions are invalidated.

The turbulence models have specified ranges of y^+ where they operate the most accurately.

2.2   Forces on hydrofoil

Hydrofoils are in principle devices for lift generation underwater. They act on the same principles as ordinary aircraft wings and the same principles and theories can be applied to them with the only difference being the density of the fluid they operate in. They are commonly used as lifting devices for hydrofoil boats where the generated lift propels the vessel out of the water thus reducing the drag.

Since the hydrofoil for the CoRMaT will be submerged in a tidal stream with a maximum stream velocity of 3 m/s and at the same time generating lift for the 10m diameter turbine, there will be a significant amount of dynamic loading on the structure. The forces acting on the hydrofoil are defined and explained in this section along with the definition of the lift, drag and moment constants.

Later, simple static analysis will be done on the forces acting on the hydrofoil and turbine to determine the seabed angle Φ for the different cases. A simple free body diagram is presented in figure 7 to clarify what the main forces on the hydrofoil are and details of these forces are given below.
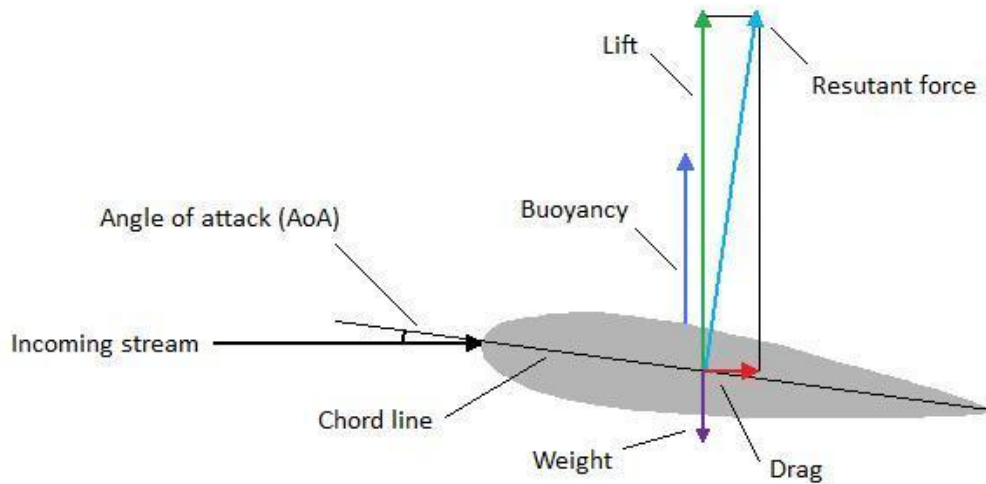
Figure 7: Main forces acting on the hydrofoil in the tidal stream.

Under the right conditions the fluid flow over an airfoil (a 2D cross section of a wing) or hydrofoil gives rise to a lift force acting perpendicular to the stream which is the main purpose of a lifting device. However, this process inevitably gives rise to a drag force which acts in parallel to the stream direction. These to forces are the constituents of the resultant force which one would feel if holding the device, this force acts perpendicular to the chord line. The lift and drag force are considered dynamic forces since they are proportional to the stream velocity which varies in a tidal stream.

In the case of the buoyant hydrofoil, a buoyant force is also present due to the difference in density of the water and hydrofoil. This force is considered static since the buoyancy does not change over the course of the tidal cycle.

2.2.1 Lift
Lift is as previously mentioned defined as the component of the force induced by fluid flow over a body acting perpendicular to the flow direction. A hydrofoil generates lift the same way as an airfoil does and this can be explained by a number of principles with varying accuracy. Two common explanations are the deflection of flow combined with Newton's equations and explanations based on the Bernoulli principle.

Newton's second and third laws of motion state that "The net force on an object is equal to its momentum change" and "to every action there is an equal and opposite reaction". This implies that when the foil exerts a force on the fluid to change its direction, the fluid exerts a force on the foil. The theory is correct in assuming that the fluid must exert a force on the wing but does not explain why the fluid is deflected.

A more accurate description comes from the Bernoulli equation which states that a when fluid with constant energy increases its velocity the pressure is lowered. This phenomenon creates a pressure imbalance on the foil since the fluid flow is faster on the top side than on the bottom which in turn creates a net force upwards. The Bernoulli equation does however not explain why the fluid travels faster at the top of the foil.

To get a full explanation on why lift is generated one must resort to the Navier- Stokes equations. In this thesis this approach will only be done by solving the Navier- Stokes equations for lift and drag using CFD.

With the lift of an object known it is possible to calculate the lift coefficient which can be useful when comparing the lift from different airfoils. It is a dimensionless coefficient that relates the generated lift of a body with the dynamic pressure of the fluid around it and a reference area on the body. It is defined as:

$$C_L = \frac{2L}{\rho v^2 A}$$

(2.32)

where L is the generated lift of the body, ρ is the fluid density, v is the fluid velocity and A is a reference area.

The lift generated by an airfoil or a hydrofoil varies by the angle of attack (AoA) and has a maximum depending on the shape of the foil. A symmetric foil generates zero lift at zero degrees AoA.

2.2.2 Drag

The drag on an object in a moving fluid is a force acting opposite of the flows direction, often causing unwanted effects in most engineering cases. The drag on a hydrofoil can be divided into two categories namely parasitic drag and induced drag.

The parasitic drag arises mainly from the interaction between the fluids particles and the hydrofoils surface and from viscous pressure drag. The parasitic drag can be thought of as an *aerodynamic friction* which is dependent on the surface smoothness and the Reynolds number of the fluid. The parasitic drag therefore increases with increasing fluid velocity.

The second form of drag arising on the hydrofoil is called the induced drag and is created by the leakage of air from the high pressure area under the foil to the low pressure area above it in a 3D flow situation. The airflow from bottom to top combined with the fluid motion twists the flow and creates tip vortices that deflect the flow behind the hydrofoil downwards. This deflects the lift vector backwards and thusly creates another drag component as illustrated in figure 8.
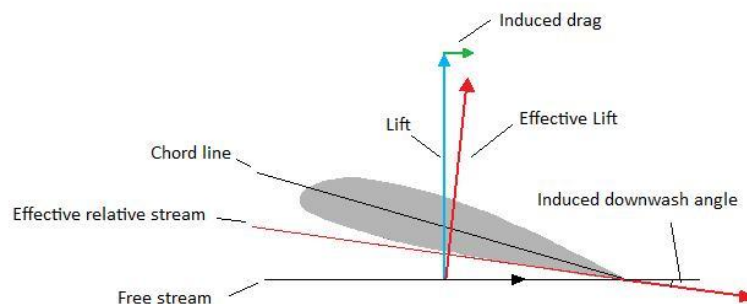
Figure 8: Diagram showing the lift and the effective lift caused by the downwash.

As opposed to the parasitic drag, the induced drag is reduced for higher stream velocities.

As for with the lift there is a coefficient for comparison between the drag of different objects, called the drag coefficient defined by:

$$C_D = \frac{2D}{\rho v^2 A}$$

(2.33)

where the constants are the same as in equation (2.33) and D is the drag force.

2.2.3 Moments

All the lift of an airfoil can be said to act on one single point called the aerodynamic centre which causes a moment on the airfoil. The moment changes with varying AoA and can cause stability issues if not considered properly. The aerodynamic centre is a point where the moment is constant for varying AoA's. A moment coefficient is defined as for lift and drag for comparison between different cases:

$$C_M = \frac{2M}{\rho v^2 AL}$$

(2.34)

where the constants are the same as above and M is the total moment and L is the moment length.

2.2.4 Buoyancy

An object immersed in a fluid experiences a greater force at the bottom of the object than at the top due to the greater hydrostatic pressure at the bottom. This gives rise to an upwards net force which is equivalent to the weight of the fluid that the object displaces and due to this reason objects with lower density have greater buoyancy. The buoyant force on a fully submerged object can be simply estimated by:

$$B = \rho_f V g$$

(2.35)

where V is the objects volume and ρ_f is the density of the fluid.

2.3 Tides

The moving of the tides can be a very powerful source of energy in some locations around the world. These high speed streams are also in many cases avoided by other users of the sea due to the hazards involved in high energy streams, which reduces the impact MCT's may have on local communities and businesses.

Tides are result of the moon's and the sun's gravitational field pulling on the Earth's water masses. The moon has the greatest influence and has a rotational period around the Earth of roughly 4 weeks and when combined with the Earth's rotation results in a tidal cycle of about 12.5h. The tidal *range*,

which is the overall difference in water level during high and low tides, varies depending on the moon and the sun's relative position to the Earth and has its maximum when the sun and the moon are on the same side of the Earth. This maximum is called a spring tide and the minimum is called the neap tide and they come in a bi- monthly cycle. These variations and the semi- diurnal variations caused by the rotation of the earth compose the velocity variations of the tidal stream. These variations are also highly predictable which is unusual for a renewable energy resource.

The gravitational effect on the Earth's oceans by the celestial bodies is illustrated in figure 9. It is the gravitational gradient between different parts of the world that causes local relative variations in the gravitational pull. If the mean is subtracted from the large vectors in figure 9, it shows the variations the short red vectors. This causes the water mass to shift accordingly.
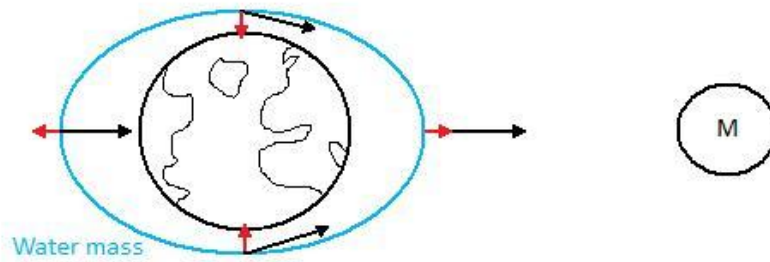
Figure 9: Exaggerated diagram of the moon's gravitational pull on the earth's water masses.

If the Earth were completely covered by water the tidal changes would not be more than 0.5m. It is the land masses that channel the water to create the large tidal ranges seen at various places around the world.

2.3.1 Sinusoidal tidal velocity

Due to the Earth's rotation and the principle described in figure 9 the tides have a approximate period of 12.5h. The semi- diurnal variation of the tidal stream velocity can therefore be said to follow a sinusoidal pattern of in and out flow. If V_{max} is the tidal current's maximal speed during a cycle and T is the period of the cycle the current velocity can be described as:

$$V = V_{max} \sin \omega t$$

(2.36)

where

$$\omega = \frac{2\pi}{T}.$$

For the calculations involving CoRMaT where V_{max}= 3m/s and T = 745 min the velocity profile over time can be viewed as in figure 10.
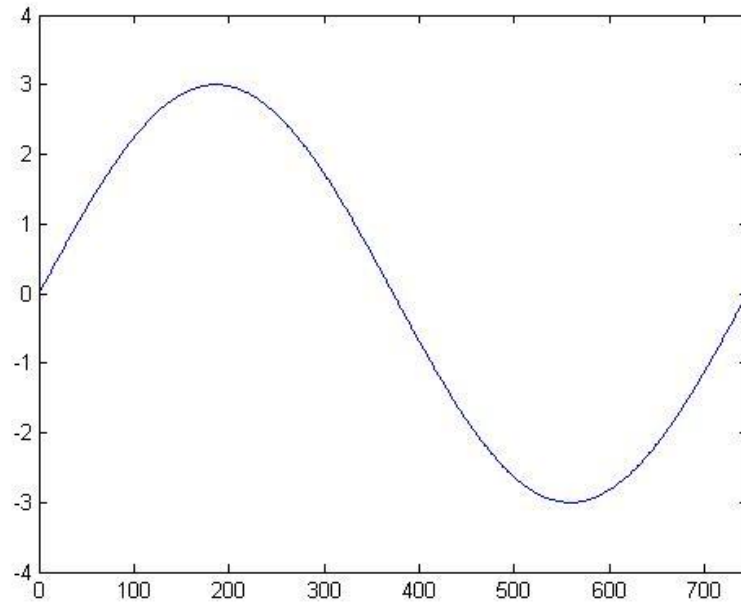
Figure 10: Tidal stream velocity time- profile for stream with 3 m/s maximum and 745 minutes period.

2.3.2 Tidal currents

Tidal currents are unstable and turbulent by nature. This is due to wave interactions coming from wind induced surface waves as well as turbulence in the current flow. Furthermore, there is a strong boundary layer interaction coming from the sea bed. The wave interactions are said to be important only if the wave flow speeds are large compared to that of the tidal stream, i.e. in extreme weather [15]. A study conducted showed that at water depths of approximately 55m the wave effects could penetrate as deep as 15m and the bottom boundary layer effects were present as far as 30m above the sea bed [16]. This leaves a narrow 10m optimal operating depth for a MCT in a 50m deep tidal stream.

Since the tidal stream is composed by several complex interactions between the diurnal and bi-monthly variations and the interactions from the surface and the bottom an approximation of the velocity profile can be done using the $1/7^{th}$ power law for turbulent velocity profiles [17].

This 1/7th power law is visualised in figure 11 where the profile is for a stream of maximum 3 m/s and the turbine has a rated flow speed of 2.5 m/s which is the maximum speed where the turbine is designed to operate. The figure assumes a depth of 100m and shows the narrow band of optimal performance and the depth needed to achieve the needed velocity.
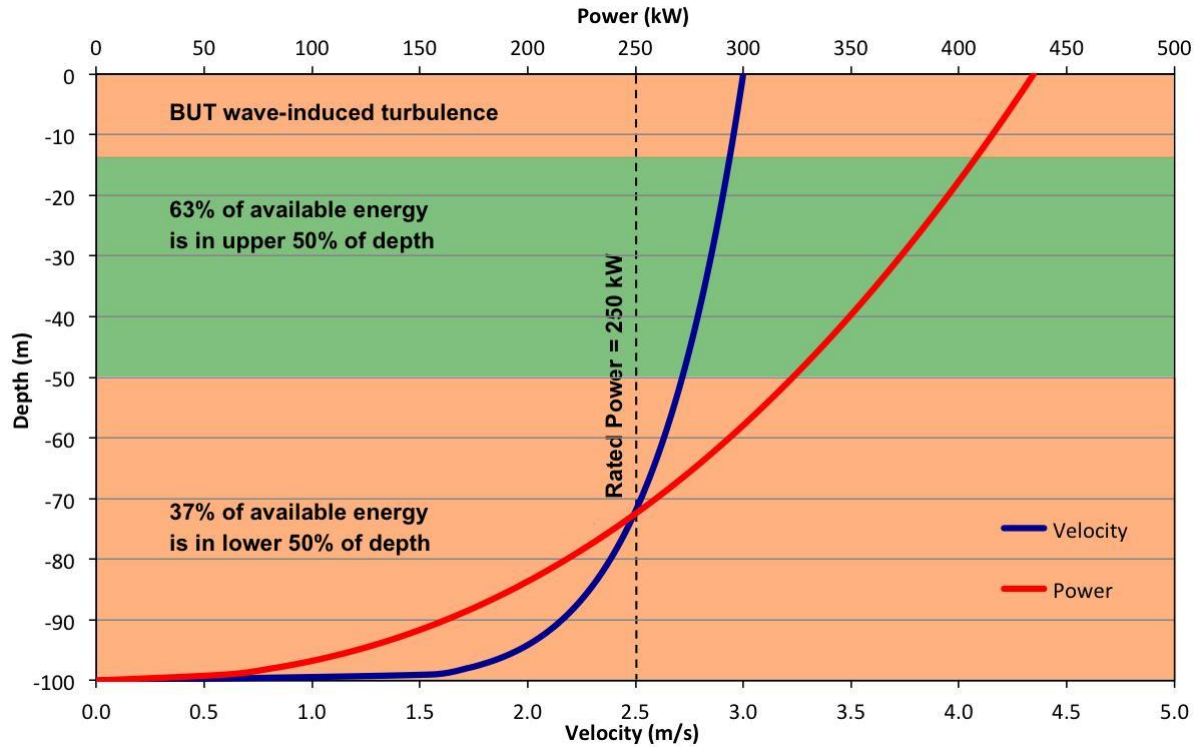
Figure 11: Diagram showing the velocity profile using the 1/7th power law approximation. Also present is the power output for a specified speed.

2.4 MCT performance

Although the flow conditions of a tidal stream are complex they are highly predictable which means that the MCT's power output also can be predicted. Through the knowledge of a specific site tidal flow conditions and the rated power output of the turbine an economic prediction can be made on the price of the wattage. If one wants to construct large arrays of turbines one must also take into consideration the footprint area of the turbine to get a prediction of the final kWh price.

2.4.1 Power generation

The power generation for a MCT at a specific site can easily be estimated by the following procedure:

Since the turbine generates power in both directions of the tidal stream and the in and out flow's time- velocity profiles are considered identical only one quarter of the cycle needs to be assessed. If the following assumptions are made about turbines, namely that the stream velocity where it starts generating power, or its cut- in velocity, is 1 m/s and maximum generating velocity, or rated velocity, is 2.5m/s. The turbine starts its generation when the cut- in speed is reached and stops the increase of power output at the rated speed by increasing the torque from the generator. The rated power of the turbine is 250kW.

The power generated by a MCT can be approximated by the following equation

$$P = \frac{1}{2} C_p \rho \pi R^2 V^3$$

(2.37)

where C_p is the power coefficient assumed to be 0.4 for the CoRMaT, ρ is sea water density at 1025 kg/m^3, R is the turbine radius of 5m and V is the stream velocity.

For a tidal stream with maximum velocity 3 m/s the power extracted from the stream using equation (2.37) for one half cycle is shown in figure 12.
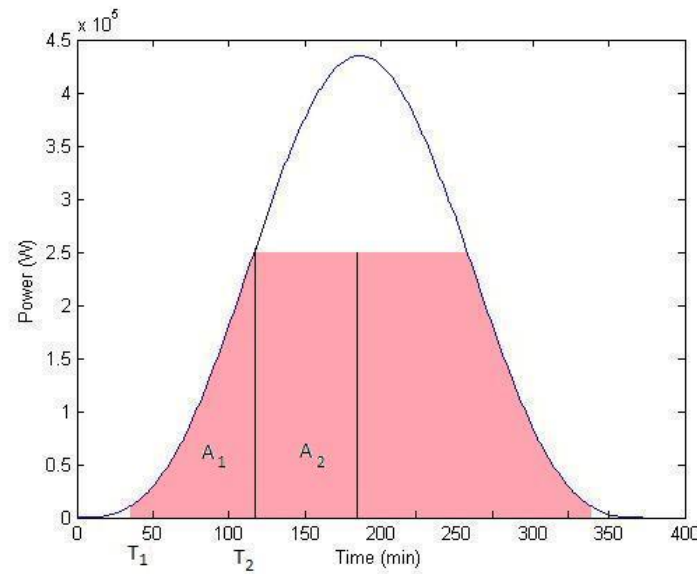
Figure 12: Graph of the available power in the stream and the extracted energy shown as the pink area. T1 and T2 denote the cut- in and rated time

To get the total energy extracted from the stream in one half cycle one must integrate equation (2.37) over the pink area in figure 12, to do this one must first know the cut- in and rated times. To get the cut- in and rated time one can rearrange equation (2.36) to

$$t = \frac{1}{\omega} \left(\sin^{-1} \frac{V}{V_{max}} \right)$$

(2.38)

while setting V to 1m/s and V_{max} to 3 m/s for the cut in time and V to 2.5 m/s for the cut out time. This gives the cut in time T_1 as 40.3 min and the rated time T_2 as 116.8 min. Substituting equation (2.36) into equation (2.37) and integrating over T_1 and T_2 gives the area A_1 in figure 12. To get area A_1 one simply multiplies the rated power P_{rated} with the time span between T_2 and half the period 372.5. The final equation for the total captured energy over one whole period with the time in seconds becomes:

24

$$E = 4 \left[\int_{T_1}^{T_2} \frac{1}{2} C_p \rho \pi R^2 V_{max}^3 \left(\sin \omega t \right)^3 dt + P_{rated} \left(372.5 \cdot 60 - T_2 \right) \right].$$

(2.39)

2.4.2   Footprint area and L/D- Φ relationship

As seen in the free body diagram in figure 7 the static analysis to determine the mooring angle Φ becomes:

$$\Phi = \tan^{-1} \left(\frac{D + D_{turb}}{B - W + L} \right)$$

(2.40)

where D is the drag on the hydrofoil determined by CFD, D_{turb} is the drag on the turbine given by rearranging equation (2.33) for D, B is the buoyancy, L is the lift from the hydrofoil determined by CFD and W is the weight of the hydrofoil.

With the maximum mooring angle known it is easy to determine the maximum swept footprint area of the turbine where the diameter can be shown by:

$$d_{footprint} = \frac{2h}{\tan(90 - \Phi)}$$

(2.41)

where h is the operating height above the sea bed.

2.4.3   Marine growth

Studies show that roughness on an airfoil close to the $1/4^{th}$ in along the chord can significantly decrease the lift to drag ratio [18]. Since the hydrofoil is at risk of being fouled by marine growth a small study was conducted on the effects of increasing the roughness of it in the CFD program. It was unclear whether the marine growth would be able to attach on the hydrofoil due to the high flow speeds around the surface but if this was the case, the cost of maintenance would rise significantly.

2.5   High lift and low drag devices

It has for a long time been standard in aircraft design to incorporate devices on airplane wings that improve the aircrafts performance during different flight conditions. There are many different types of devices that can alter the wings performance by for example increasing lift or changing the stall characteristics of the wing. There are also devices that can reduce the induced drag on a wing as described in section 2.2.2.

The devices that were considered for the hydrofoil in this thesis were the trailing edge flap and end plates, or winglets, described below.

2.5.1   Flaps

There are many different types of flaps employed in modern aircraft design. The most common ones are the trailing edge flap and the leading edge 'slat'. The purpose of a flap is to increase the lift and

drag on a wing and alter the stall angle to allow safer speeds and descent angles when landing. This is achieved by the flap altering the camber line of the foil which increases C_L and in some cases also increasing the surface area. The increase in lift also increases the induced drag and one objective of the CFD study was to see if there was a net gain of L/D ratio from adding a flap.

Two types of trailing edge flaps that were considered were the plain flap and the slotted flap shown in figure 13. Unfortunately, the CPU cost was too high for analysis of the more efficient slotted flap and analysis was restricted to the plain flap.

Figure 13: Two common trailing edge flap configurations.

2.5.2   End plates

Since the suggested geometry of the hydrofoil has low aspect ratio it could be suspected that the induced drag due to trailing vortices would be high. A measure of mitigating this effect was to ad so called end plates at the short sides of the hydrofoil. These end plates reduce the induced drag by recovering energy from the tip vortices and giving the flow over the hydrofoil a more '2- dimensional character'. Wind tunnel data from previous experiments suggests that circular or elliptical end plates give the best decrease in drag while being relatively simple to construct.

3   Methods

To determine a suitable geometry for the hydrofoil that would yield the smallest mooring angle, the study was divided up in to two cases: One 2D case where the L/D ratio was compared for different foil shapes at different AoA and one 3D study where the selected foil was given an appropriate width and the 3D flow characteristics were studied for different AoA. Some meta- studies were also conducted to verify the accuracy of the CFD studies which included mesh- independence studies and model verifications. Finally an investigation on the effects of increased roughness on the hydrofoil by marine fouling was conducted.

With the L/D ratios known for the different geometries, a Matlab script was created to quickly and easily perform the static analyses of the hydrofoils in order to get the mooring angles.

3.1   CFD Simulation approach

All of the simulations in this thesis were done in Fluent 6.3 run through the ANSYS 12 workbench. The software setup was done in a way to replicate the flow conditions in a tidal stream as accurately as possible in a *Steady State* case. Every geometry was also studied for a range of AoA's in the maximum stream velocity of 3m/s since this velocity will determine the largest mooring angle in the tidal cycle.

For the 2D study a number of suitable hydrofoil profiles were chosen for investigation and the one with the highest L/D ratio was further investigated in the 3D run. In the 3D run the selected foil was modelled as a full scale hydrofoil and a flap and end plates were added in a later stage. To save CPU resources a symmetry plane was defined along the 3D geometries mid section as described below.

3.2 2D study

The 2D study was performed as a CPU inexpensive way of determining the most suitable foil shape for operating AoA's between 0 and 10 degrees in 3m/s flow. The parameters compared were the lift, drag and moments of the geometries.

3.2.1 Geometries

The 2D geometries were modelled by obtaining airfoil vertex data from a web source [19] and using the built in ANSYS Designmodeler to create a polyline between the points. The flow domain was then defined as a C- domain area (figure 14) with 12.5 chord lengths to every far field boundary. An area was then created with the polyline as boundary and subtracted from the flow domain. This process was repeated for all the different airfoil profiles. The foils were scaled to have a chord length of 7m determined from a static analysis using the Matlab code and lift and drag approximations from equations (2.32) and (2.33).
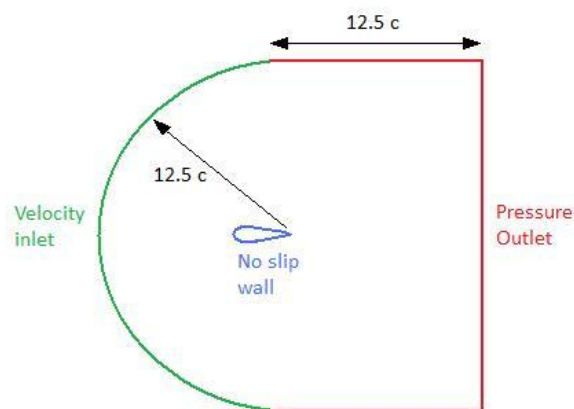
Figure 14: Diagram showing domain definition and boundary conditions

3.2.1.1 Foil profiles

The suitable airfoil profile candidates had to conform to a set of criteria to be chosen. Firstly, all the investigated foil profiles were thick (25% of chord length thickness) to be able to allow for maximum buoyancy and structural integrity. Secondly, only symmetrical foils were selected since it was believed that their construction complexity and cost would be less. The drawback with thick foils is that they have larger parasitic drag but an advantage can be that the lift curve slope decreases, giving greater pitch stability.

Four foil profiles were finally selected for CFD analysis. These were the following:

NACA0025

This foil shape was created by the predecessors to NASA, namely NACA. The number denotation indicates that the foil has 25% of the chord length maximum thickness and has no chord camber. The NACA0025 is thick and robust and due to its thick trailing edge it was considered the cheapest one to manufacture.

NACA0025-72

This foil was a modification of the NACA0025 with a slightly thicker leading edge or blunter nose. This modification was believed to give the foil better lift as seen in experimental data [18]. The profile was created using JavaFoil and the parameters were a 10% radius of the leading edge and the maximum thickness was located 25% in on the chord.

Joukowski 25%

The Joukowski foil was selected to investigate the performance of a foil similar to the NACA0025 but with a thinner trailing edge. The foil had to be scaled up in the y- direction to get the 25% maximum thickness. It was believed to be the hardest foil to manufacture due to its sharp trailing edge.

Eppler E838

The Eppler E838 was the only foil selected originally designed to be a hydrofoil. The geometry is very close to symmetrical and it has a maximum thickness of 18%. The lack of buoyancy of this foil was hoped to be compensated by its greater lifting capabilities.

Images of the aforementioned foils can be found in Appendix 7.

3.2.2   Mesh

The meshes for the 2D runs were created in the ANSYS Meshing Application and used structured grids. The grid structure was defined by dividing the pressure outlet domains into 120 cells per line and the inlet domain to 240 cells. A bias factor was set on the lines towards the hydrofoil geometry and set to 700. This gave meshes with approximately 87000 nodes with the highest node density near the hydrofoil.

3.2.3   Simulation setup and software settings

For every hydrofoil profile 6 simulations had to be done for AoA's 0, 2, 4, 6, 8 and 10 degrees by rotating the mesh between runs. The boundary conditions were set up as in figure 14 where the velocity at the inlet was set to 3 m/s and the turbulent intensity was set to 3% and the turbulent length scale was set to 1m. The same turbulent conditions were given to the pressure outlet where the static pressure was set to 0pa. The walls of the hydrofoil were given no- slip conditions and were considered completely smooth.

A new fluid had to be defined as sea water with the only parameters needed for the governing equations (section 2.1.1.1) being density and viscosity set to ρ = 1025 kg/m^3 and μ = 1.307e-3 Ns/m^2.

A pressure based solver was selected and the Transitional SST k- ω model was selected as turbulence model under the incorrect belief that it would resolve the laminar separation (discussed in verification results).

A second order solving scheme was employed for greater accuracy and the courant number was lowered to 20 for a more stable solution. The convergence criteria were set to 1e-6 for all measurable parameters and the maximum amount of iterations were set to 2000. The settings for the solver can be seen in table 1 below:

Table 1: Settings for the 2D solver

Option	Setting
Pressure velocity coupling	Coupled
Gradient	Least squares cell based
Pressure	Standard
Momentum, turbulence, specific	2:nd order upwind
Courant nr	20
All relaxation factors	0.5
Convergence criteria	1e-6

3.2.4 Mesh independence study

A mesh independence study was conducted to verify that the solution given was not dependant on the resolution of the mesh. The parameters of interest were the lift and the drag coefficient. Four different meshes were studied for the NACA0025 profile at 8 degrees AoA each with the same structured formation but with varying node numbers which were 87120, 118440, 135900 and 154560 nodes.

3.2.5 Verification of model

As with all CFD analysis the methods have to be verified to consistent with reality to give any confidence in the results.

In the first attempt to verify the 2D model the results of lift and drag for a NACA0025 profile with Re= $3 \cdot 10^6$ were compared to those found in wind tunnel data. The resulting lift and drag curves were plotted against the AoA's and the drag coefficients were found to be lower than the experimental data. Later it was realised that FLUENT 6.3 uses a fully turbulent flow and no laminar boundary layer is present if not specified in the SST k- ω model. This causes the under prediction since the wind tunnel experiment had laminar flow and boundary layer separation which increase the drag.

Therefore, the drag coefficients were compared to fully turbulent data using tripped flow over an NACA0012 profile and with similar Reynolds numbers at 0 degrees AoA. A corresponding geometry was created and simulated with the same parameters as in the wind tunnel and the study and gave accurate results.

3.3 3D Study

The 3D case was conducted to study the 3- dimensional effects of the flow over the selected 2D-geometry. Since the 3D simulation takes 3D effects into consideration it gives a more accurate lift and drag estimation and a more accurate mooring angle. Furthermore, the trailing vortices were studied and the effectiveness of the end plates was assessed.

3.3.1 Geometries

NACA0025

All the geometries were modelled using GAMBIT and the far field boundaries were set to be 12.5 chord lengths away from the hydrofoil. The flow domains were created first and the hydrofoil volume was subtracted from this using a Boolean operation. Since the flow over the hydrofoil is symmetrical in the x-y-plane only half of the geometry was constructed and two symmetry planes were set as in figure 15.
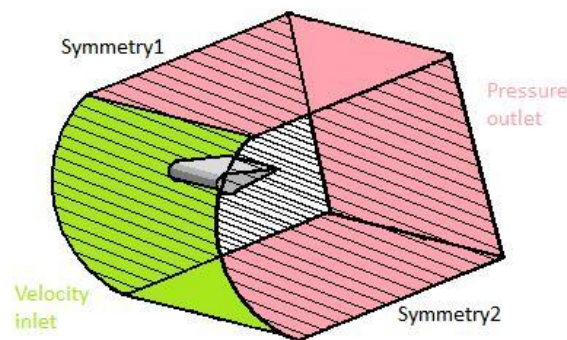

Figure 15: Not to scale diagram of the 3D geometry modelled by applying symmetry conditions on the x-y boundary planes.

The geometry of the hydrofoil was created by extracting the NACA0025 profile 8.5m in the z-direction to make up half of the 17m wide hydrofoil. The measure of 17m was derived using the Matlab script in Appendix B. The method of determining the dimensions was simply trial and error by varying the length and width of the hydrofoil until a satisfactory estimation was found.

Trailing edge flap

The geometry of the hydrofoil with a flap was created by rotating the 20% of the chord closest to the trailing edge 20 degrees downwards. The volume was then extruded in the same way as for the NACA0025 geometry.

End plates

End plates were added to two NACA0025 geometries to compare how they changed the efficiency of the hydrofoil.

Two geometries were constructed for the end plates one being a circle with the diameter of the foil chord of 7m and a thickness of 0.1m. The second geometry was elliptic end plate with the centre half way down the chord line (3.5, 0.0, 8.59997) and a semi- major axis of 3.5m to cover the entire foil. The semi- minor axis was set as $1/5^{th}$ of half the foil thickness to give a coordinate of (3.5, 4.375, 8.59997).

3.3.2 Mesh

The meshing of all the 3D geometries was done in GAMBIT and used an unstructured scheme. A size function was applied to the hydrofoil boundary to generate a higher node density around the foil. The settings of the size function were a minimum cell size of 0.002m and maximum cell size 3m. A growth factor of 1.6 was applied to the size function to give meshes with around 2 million nodes for every geometry. Details of the geometries mesh sizes can be seen in table 2:

Table 2: The number of nodes in each used mesh.

Geometry	Number of nodes
NACA0025	2160656
NACA0025 Flap	2177315
NACA0025 Circular end plate	2715391
NACA0025 Elliptical end plate	2573178

3.3.3 Simulation setup and software settings

The simulation was set up in the same manner as in section 3.2.3 with the differences that there were symmetry planes defined at the x-y boundary planes. Furthermore the SST k- ω was used in the 3D runs as it was considered more computationally cheap and reliable in a 3D case. The mesh was rotated as in the 2D case but an extra AoA at 14 degrees was also included.

The reference area given for the calculation of the coefficients was half of the plan form area namely $59.5 m^2$.

3.3.4 Mesh independence study

A mesh independence study was conducted for one of the 3D meshes to prove that the solutions were not mesh dependant. The mesh chosen for the study was the plain NACA0025 mesh at 8 degrees AoA with a large range of node numbers. The investigated values were the lift and drag coefficient.

3.3.5 Verification of model

The model was verified in a similar way as for the 2D case by comparison with tripped wind tunnel data but using SST k- ω turbulence model. The results can be found in the next chapter.

3.4 Marine growth

The selected NACA0025 profile was subjected to a proof- of- concept like roughness study in 2D to prove that marine growth could have an impact on the hydrofoil performance at 8 degrees AoA. This was done by changing the roughness heights for the hydrofoils walls with values of 0, 0.01, 0.02, 0.03 and 0.04m. The roughness constant was set to 0.5 which implies a uniformly spread roughness.

The assumption of marine growth height was derived by the aforementioned student team at Strathclyde University. Details of the investigation can be found at:

http://www.esru.strath.ac.uk/EandE/Web_sites/11-12/MORE/enviornmental/marine_growth.html

3.5 Matlab script

A simple Matlab script was written to save the effort of computing every static analysis equation by hand for all of the geometries. The script calculates the buoyancy and the weight of the hydrofoil and uses the lift and drag derived from the CFD runs to return a mooring angle. The script is parametric so the density and dimensions of the foil can be easily changed, although the script will naturally not take the varying 3D flow effects into account.

The assumption of the hydrofoils density is 500kg/m^3 and the chord length is 7m and the width is 17m as previously mentioned. The script can be seen in Appendix B where the experimental data is imputed for 8 degrees angle of attack.

The density of the end plates is set to 700 kg/m^3 due to the addition of support structures inside.

4 Results

This chapter presents the results of the different CFD studies and gives comparison between the different configurations performances. Firstly, the results from the verification are presented. All the numerical data can be found in Appendix D.

4.1 Verification

With the knowledge that the flow around the hydrofoil in the tidal stream should be considered fully turbulently developed the results were as presented below.

4.1.1 2D

The results for the lift coefficient verification for the NACA0025 at Re= $3 \cdot 10^6$ are shown below (figure 16). The y+ range for all the verification studies was in the range of 47 to 95.
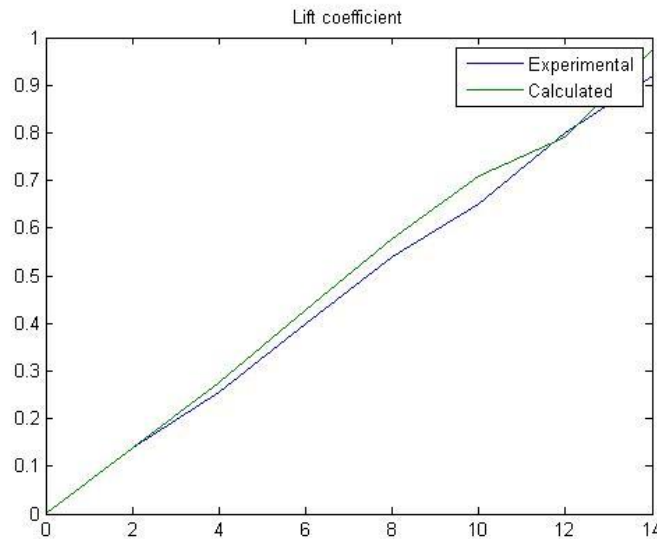

Figure 16: Lift coefficient for experimental and calculated data for different AoA's.

The under predicted drag from the NACA0025 run as compared to laminar flow wind tunnel data is shown in figure 17.

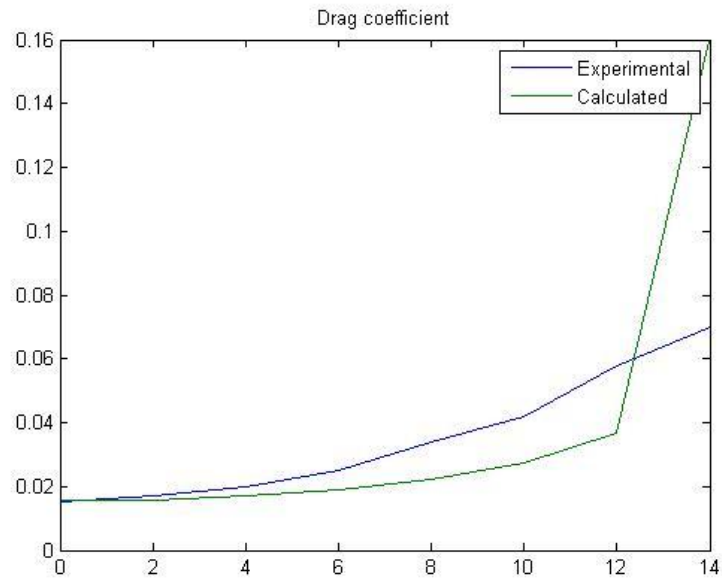**Figure 17: Under predicted drag coefficient as compared to experimental laminar flow wind tunnel data.**

The results for drag coefficients for the NACA0012 foil compared to tripped turbulent wind tunnel data for the same geometry is shown in table 3.

Table 3: Drag CFD results and experimental data.

Experimental Cd	Calculated Cd	Reynolds Number
0.0087	0.009533	4*10^6
0.0077	0.008421	10^7

4.1.2 3D

The turbulence model for the 3D case was verified in a similar way as the 2D model using a 2D setup. The results are presented in figure 18 and figure 19.
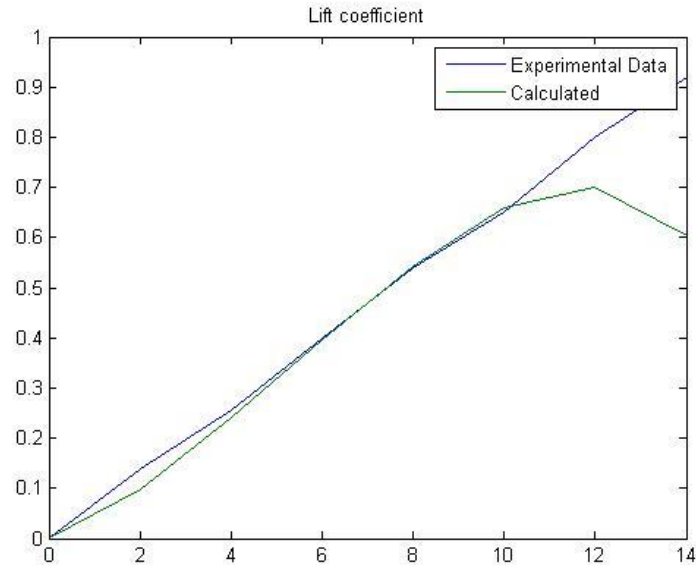

Figure 18: Experimental lift coefficient data and calculated lift coefficient.
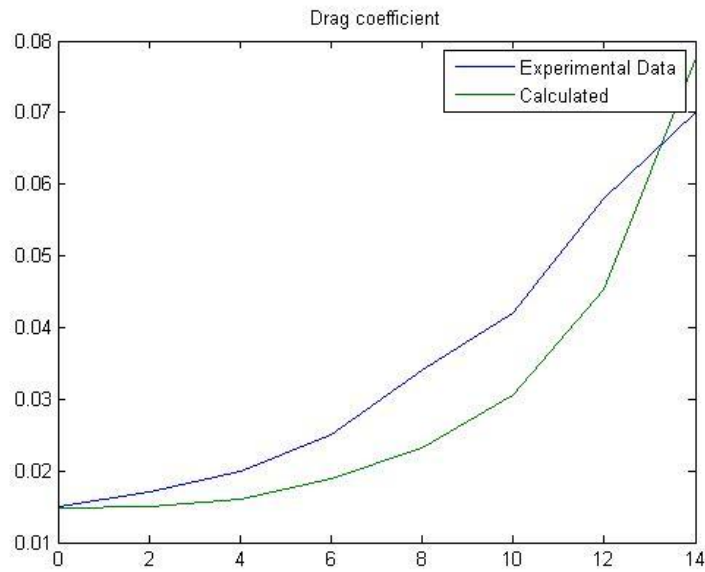

Figure 19: Experimental drag coefficient data and calculated drag coefficient.

4.2 Mesh independence

The results of the mesh independence studies are plotted below in figures 20 and 21. The C_L and C_D are plotted against the number of nodes in the mesh.

4.2.1 2D
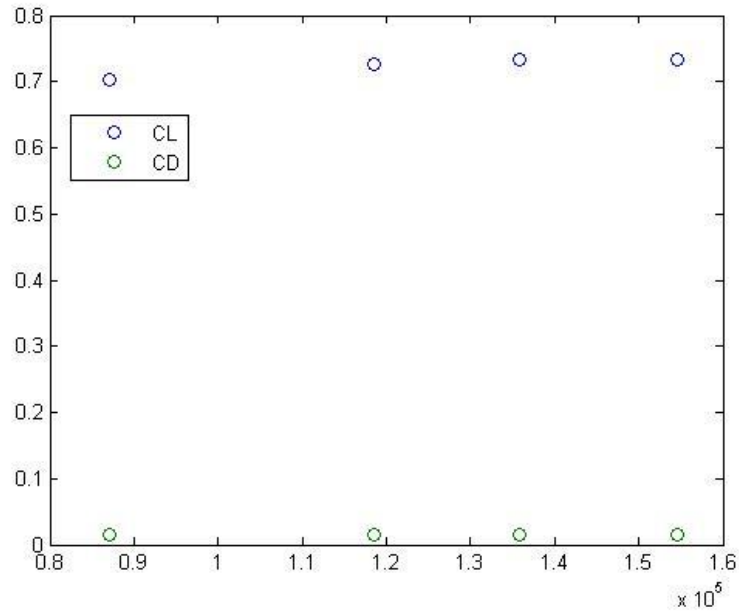
Figure 20: Graph of CL and CD plotted against number of nodes in the computational grid for the 2D case.

4.2.2 3D
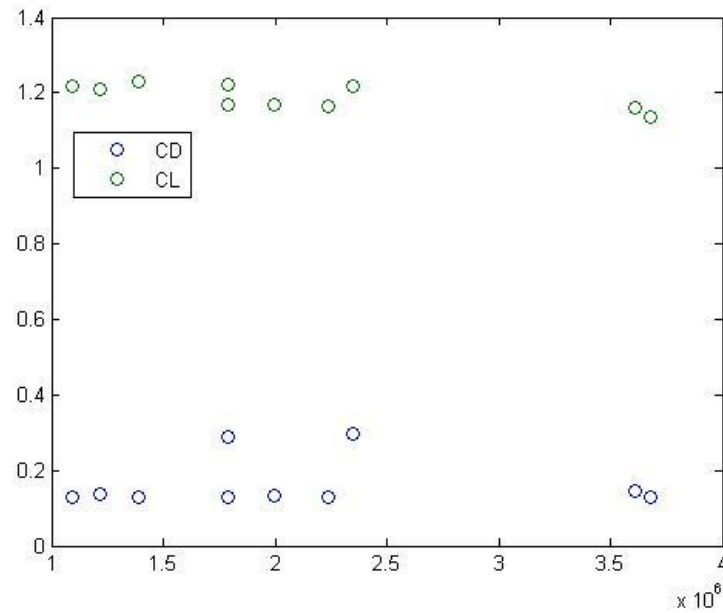
Figure 21: Graph of CL and CD plotted against number of nodes in the computational grid for the 3D case

4.3 2D Results

The results from the comparative 2D study are presented in this section. The calculated values of C_L, C_D and C_m are plotted against the AoA for all the different foil profiles. The L/D ratio, which is a measurement of how effective the lifting device is, is also plotted against the AoA. The mooring angles given from multiplying the calculated L and D forces by the width 17 are presented in table form.

35

4.3.1 Coefficients plotted against AoA

The lift and drag coefficients for every foil shape are given below along with the L/D ratio. The moment coefficients are also shown (figures 22, 23, 24 and 25).

Figure 22: Lift coefficients plotted against AoA in the 2D case.

Figure 23: Drag coefficients plotted against AoA in the 2D case.

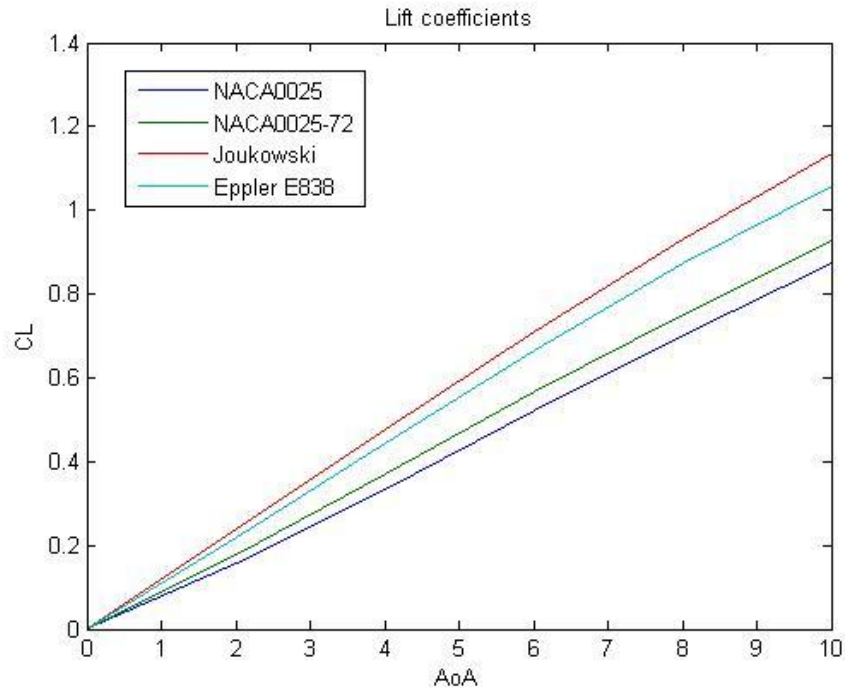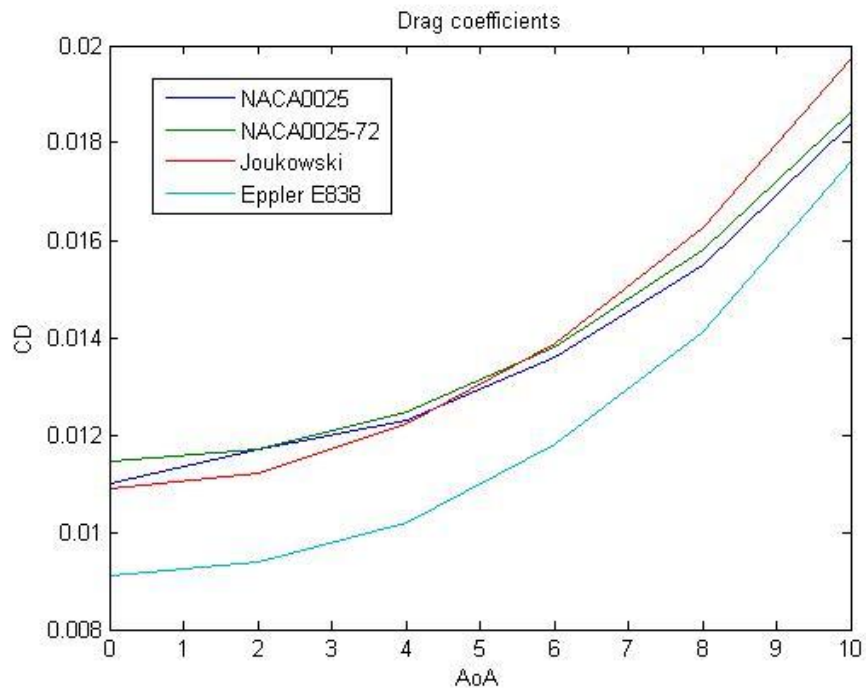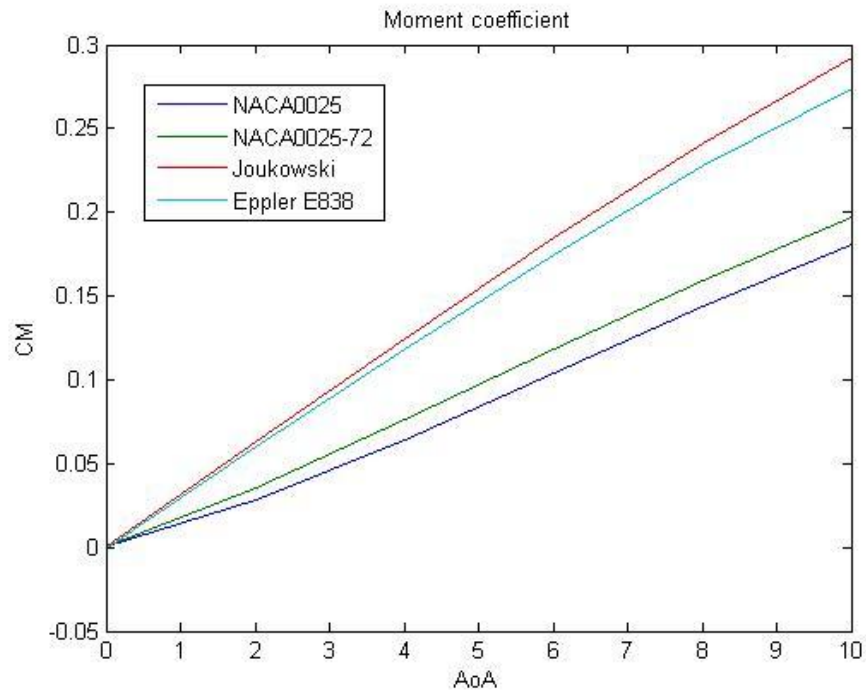**Figure 24: Moment coefficients plotted against AoA in the 2D case.**
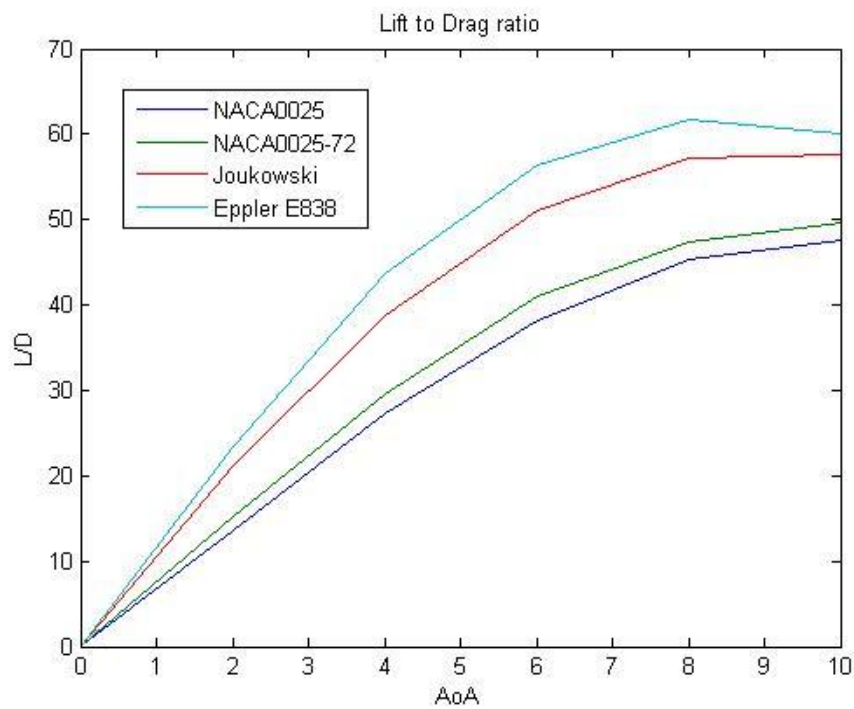

Figure 25: Lift to drag ratios plotted against AoA for the 2D case.

4.3.2 Calculated mooring angels

Using the Matlab script it was possible to get an estimation of the mooring angles for the 2D case. Since the 2D case calculates all the values in 'per meter in z- direction' one must multiply all values with 17 before entering the values to the script. The 2D case does also not take into account the 3D flow effects therefore the mooring angles are expected to be less than in the 3D case. The angles are presented in table 4 from best to worst and a ratio of buoyancy to lift is also given. The AoA for the hydrofoils is 8 degrees for the maximum L/D ratio.

Table 4: Mooring angles for the different 2D profiles along with the hydrofoils buoyancy to lift ratio.

Foil profile	Mooring angle Φ	Buoyancy to lift ratio (B/L)
Joukowski 25%	26.92	0.1831
Eppler E838	29.60	0.1483
NACA0025-72	31.39	0.2533
NACA0025	32.07	0.2704

4.3.3 Roughness study

The results from the proof of concept roughness study are presented in this section. The lift and drag coefficients for the NACA0025 profile at 8 degrees AoA are plotted against the roughness height in figure 26.
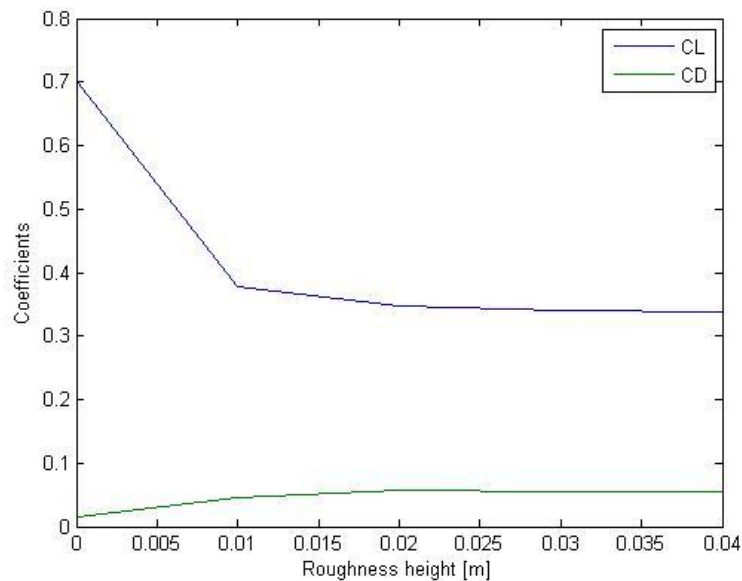
Figure 26: Lift and drag ratio for the NACA0025 in 8 degrees AoA for varying roughness heights.

4.4 3D Results

As for the 2D case the calculated coefficients are plotted against the AoA's for every geometry in figures 27 to 30. The Matlab script was used to determine the mooring angles presented in table 5. The motivation for which geometries were selected for 3D analysis was based on the 2D results and can be found in the next chapter.

The results for the geometries with trailing edge flaps are presented separately for clarity in figures 31 to 34.

4.4.1 Coefficients plotted against AoA

Figure 27: Lift coefficients plotted against AoA for the 3D case.

Figure 28: Drag coefficients plotted against AoA for the 3D case.

Figure 29: Moment coefficients plotted against AoA for the 3D case.

Figure 30: Lift to drag ratios plotted against AoA for the 3D case.

The results for the geometries with trailing edge flaps are presented below. The range of AoA's for these geometries ranged from -8 to 14 degrees.

Figure 31: Lift coefficients plotted against AoA for the 3D case with flaps.
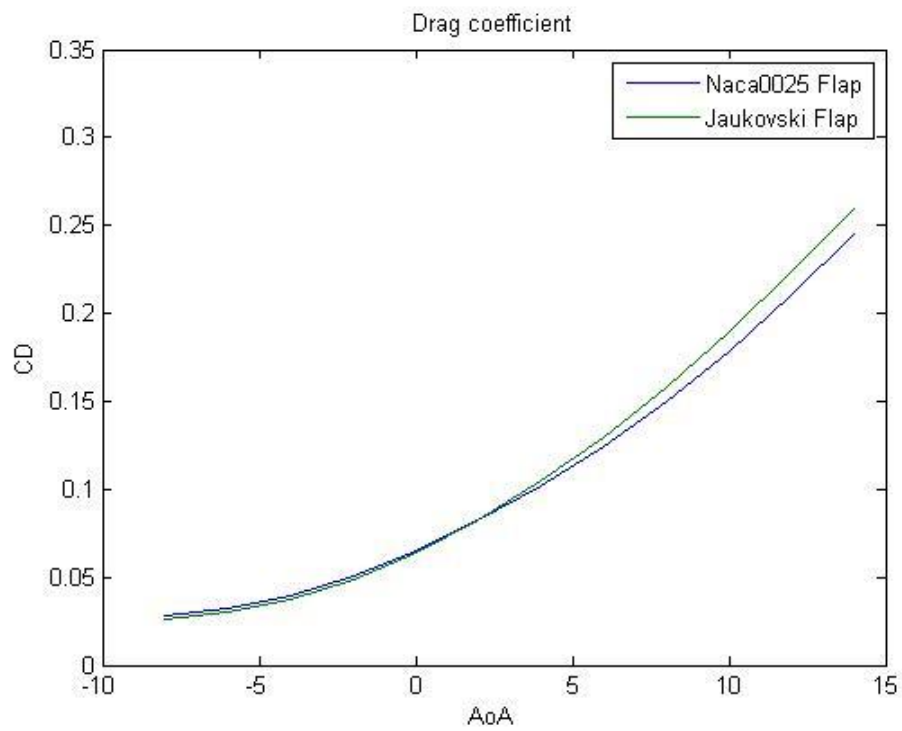
Figure 32: Drag coefficients plotted against AoA for the 3D case with flaps.

41
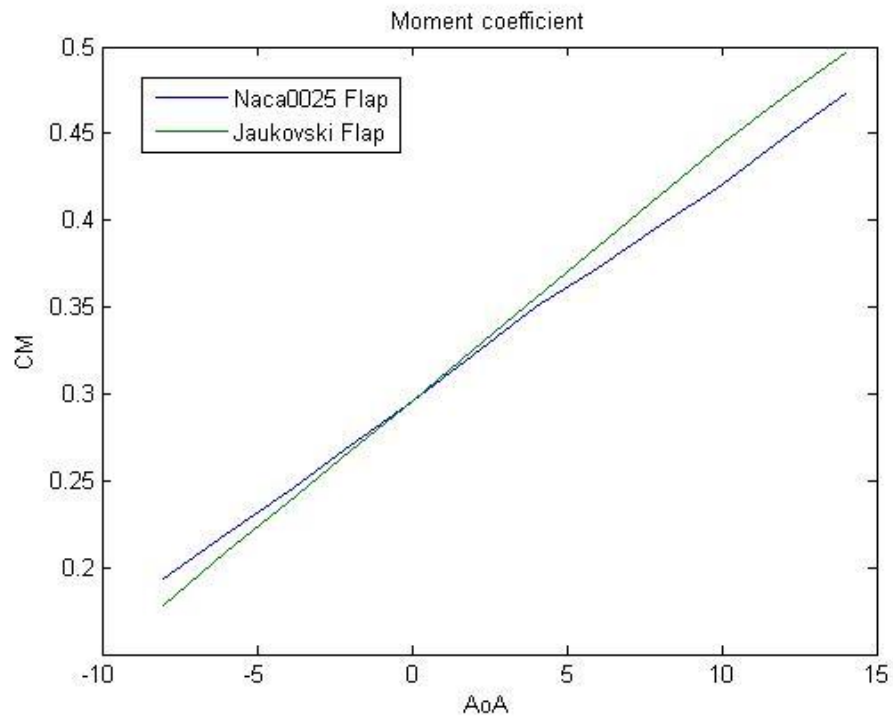
Figure 33: Moment coefficients plotted against AoA for the 3D case with flaps.

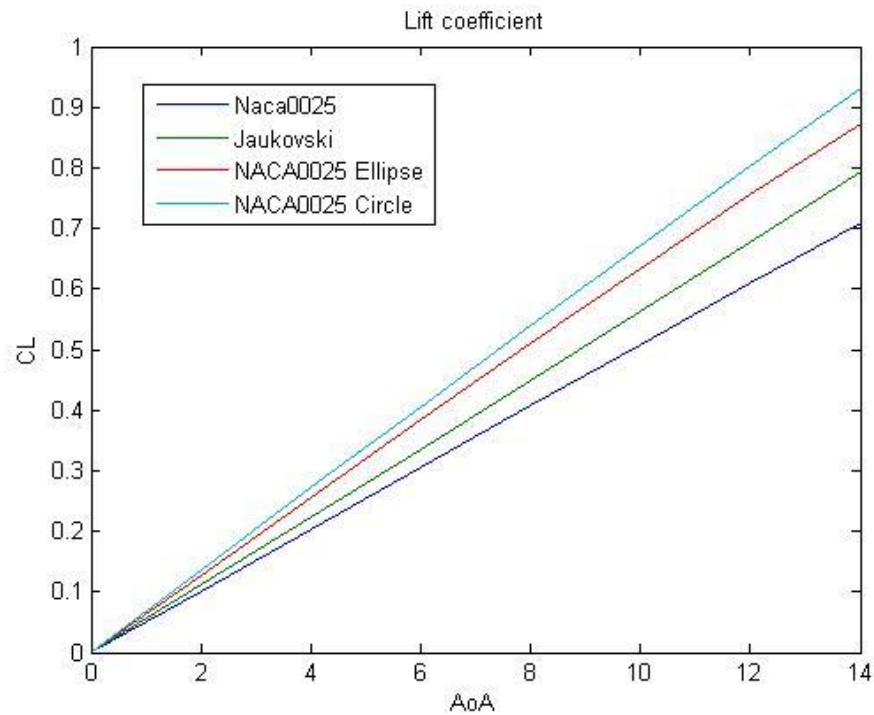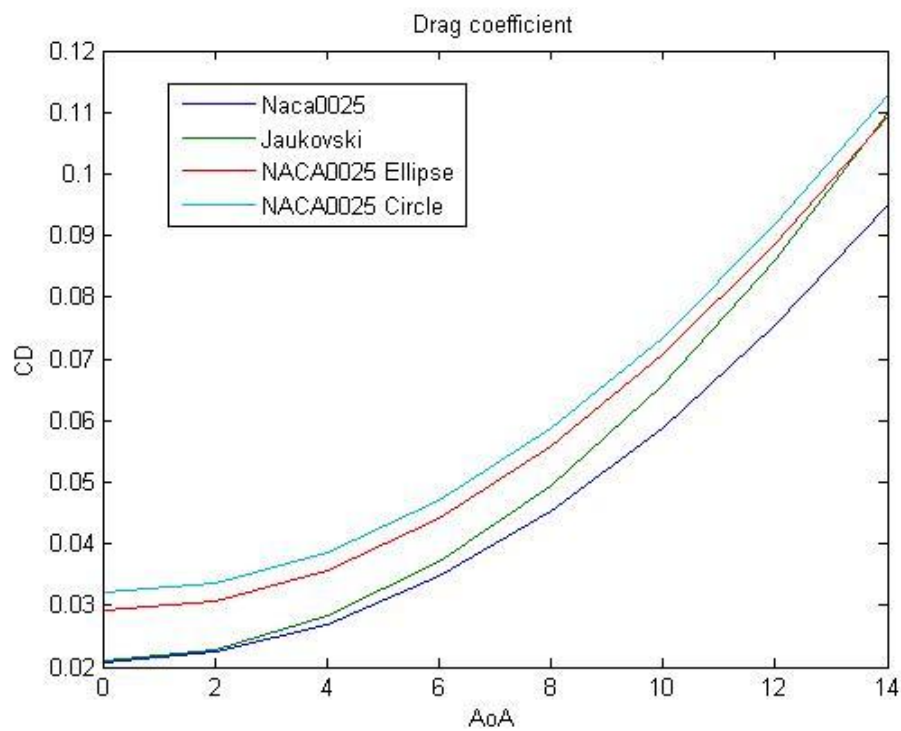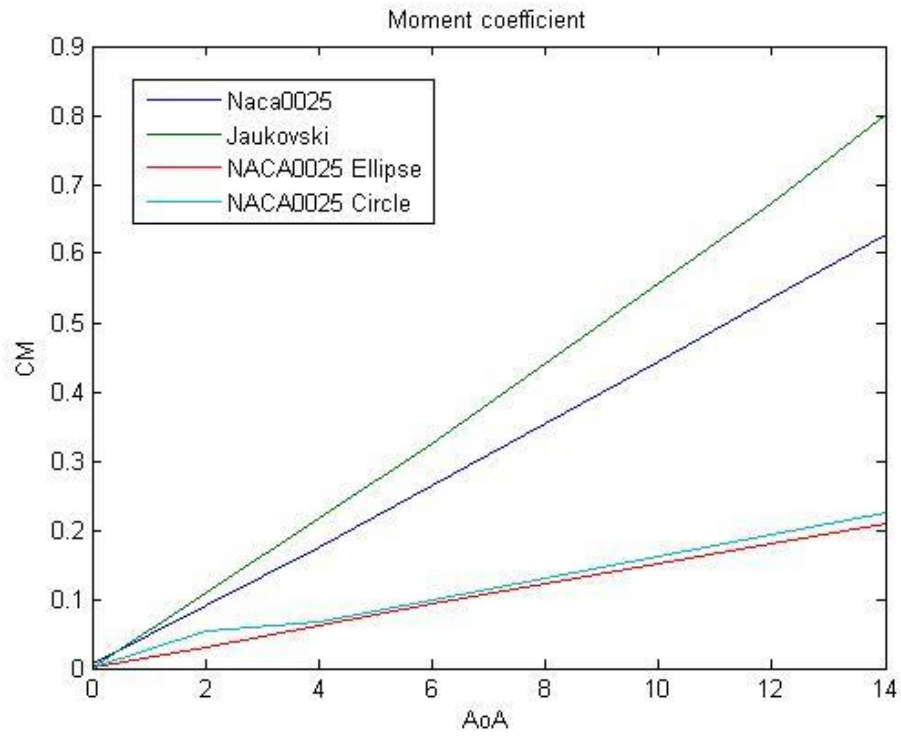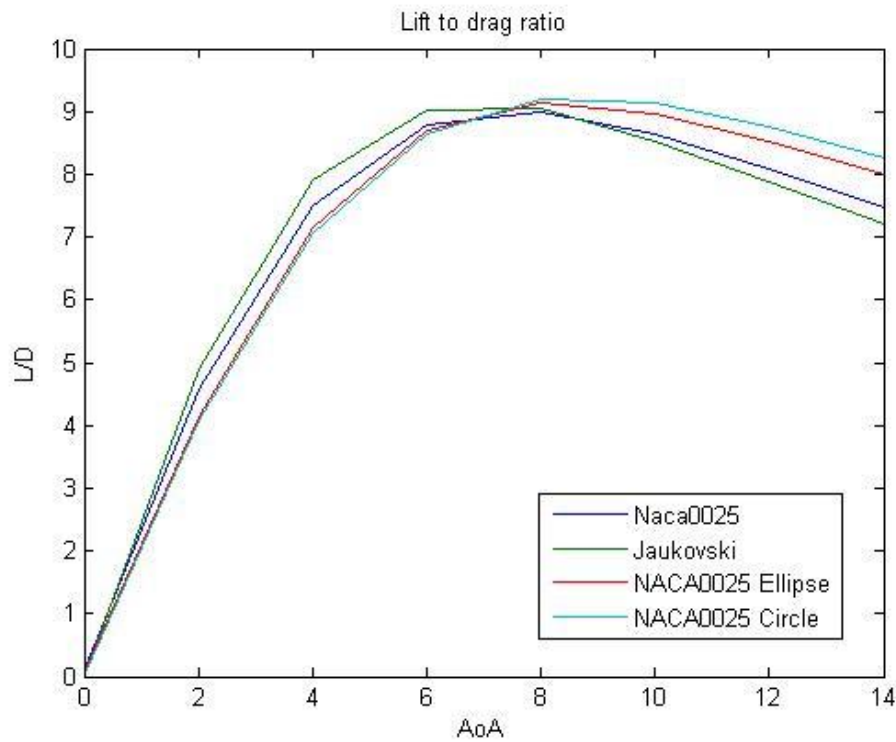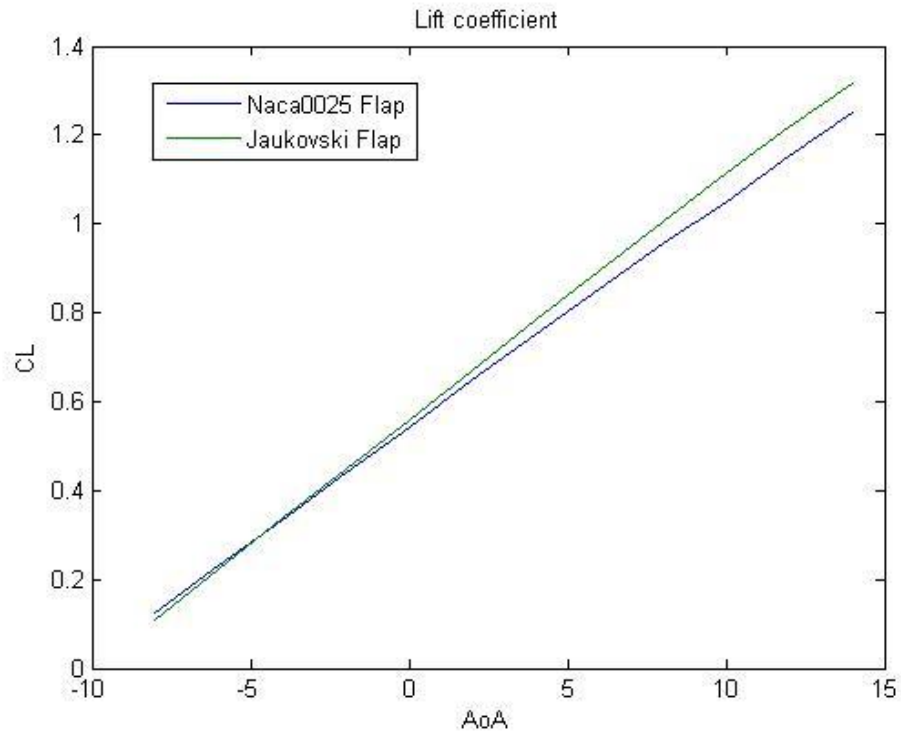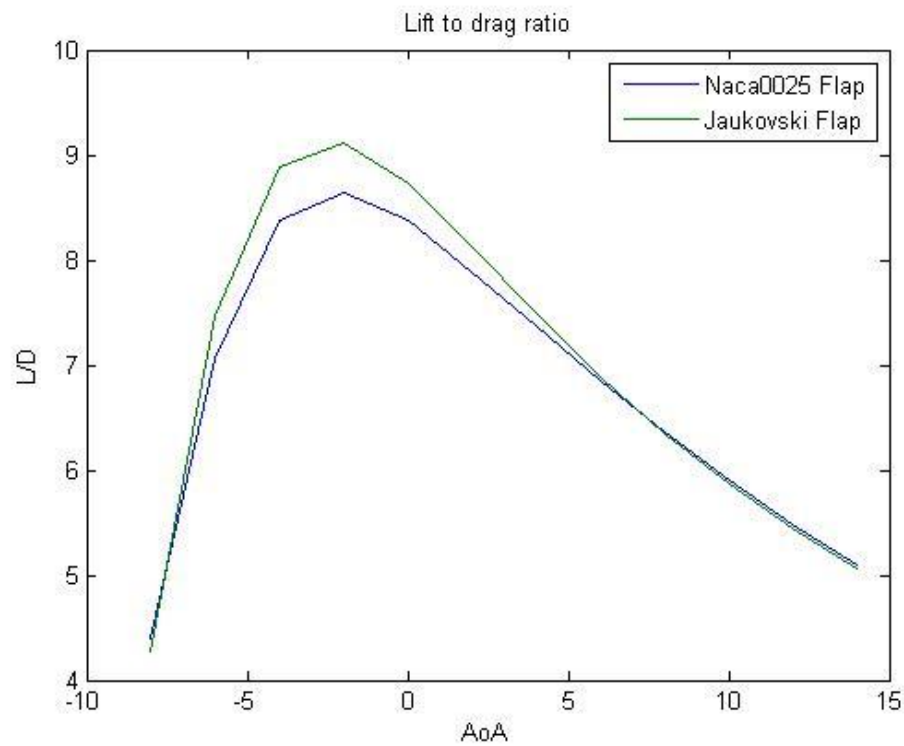**Figure 34: Lift to drag ratios plotted against AoA for the 3D case with flaps.**

4.4.2 Calculated mooring angles and footprint areas

As for the 2D case the mooring angles were calculated for each geometry and presented from smallest to highest in table 5. The angles were expected to be larger than for the 2D case since the 3D simulation had taken the induced trailing vortices into account. The AoA's for the hydrofoils were taken as 8 degrees again for maximum L/D ratio, except for the flap geometries were the AoA was -2 degrees. The footprint diameters were calculated using equation (2.41) and assuming that the turbine had an operating height of 50m.

Table 5: Mooring angles, footprint areas and B/L ratios for the 3D geometries.

Foil profile	Mooring angle Φ	Footprint diameter (m)	Buoyancy to lift ratio (B/L)
NACA0025 Circular Plate	38.49	79.51	0.4149
NACA0025 Elliptic Plate	39.88	83.55	0.4382
NACA0025 Flap	43.98	96.50	0.4316
Joukowski 25% Flap	44.44	98.06	0.3811
Joukowski 25%	44.46	98.13	0.3811
NACA0025	45.24	100.84	0.4661

4.4.3 Trailing vortex reduction

The reduction of the induced trailing vortices by the end plates is presented visually and with numerical data below. The pressure profiles are plotted on a surface 1m behind the different hydrofoils with end plates and for the plain NACA0025 for comparison of the vortices.

The pressure distributions 1m behind the NACA0025, the NACA0025 with elliptical end plate and the NACA0025 with circular end plate are shown in figure 34, figure 35 and figure 36.

For images of the velocity and turbulent kinetic energy see Appendix C
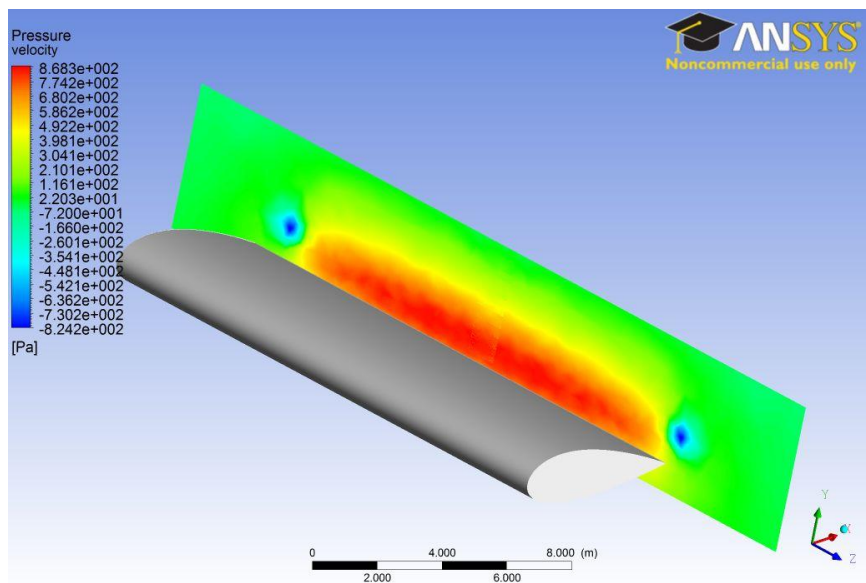
Figure 35: Pressure distribution plotted 1m behind the NACA0025 profile. Two distinct low pressure areas are seen in the trailing vortices.
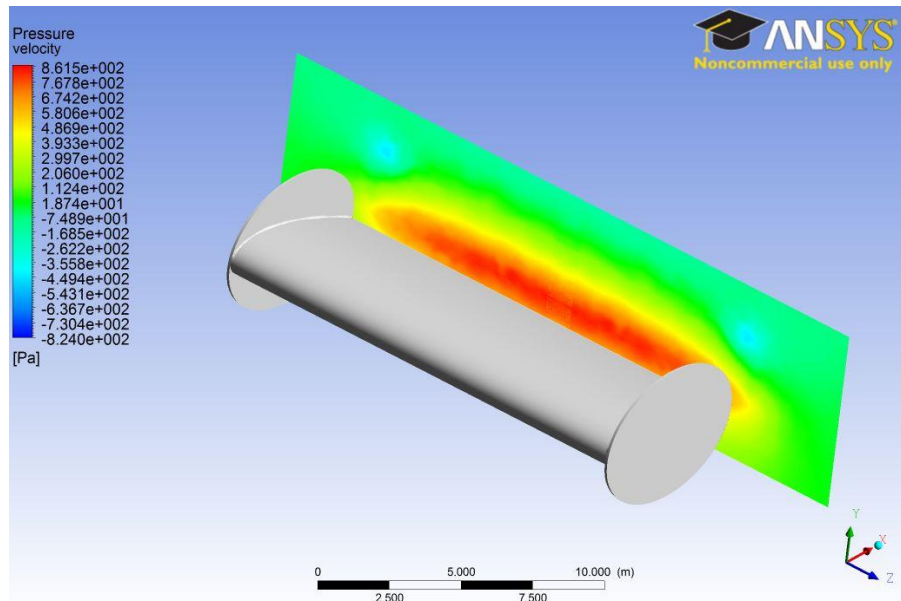
Figure 36: Pressure distribution plotted 1m behind the NACA0025 profile with elliptical end plates. Two low pressure areas are seen in the trailing vortices.
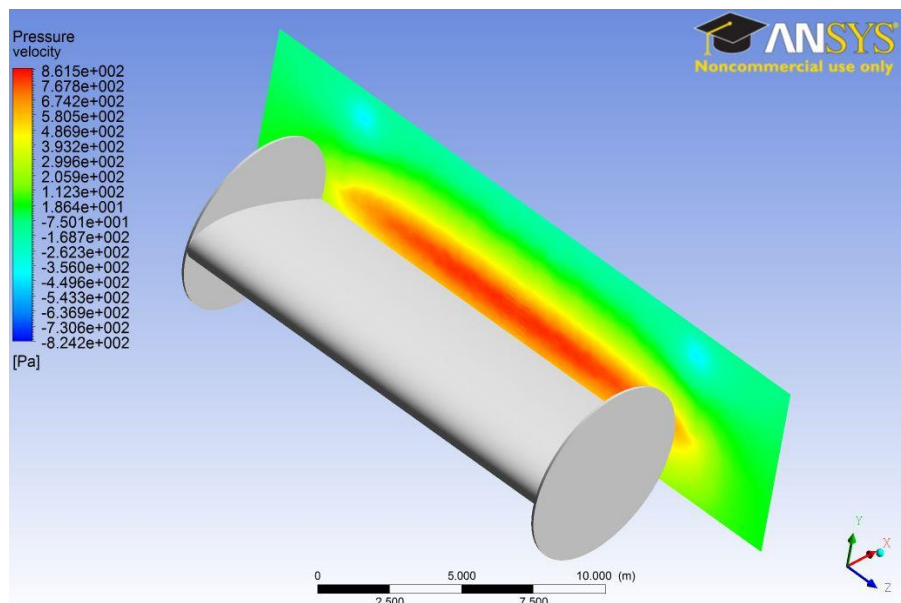
Figure 37: Pressure distribution plotted 1m behind the NACA0025 profile with circular end plate. Two low pressure areas are barely seen in the trailing vortices.

The numerical values for the pressure, velocity, turbulent kinetic energy and the velocity curl in the centre of the trailing vortices 1m behind the hydrofoil are given in table 6.

Table 6: Values for the trailing vortex centres 1m behind the geometries.

Geometry	Velocity [m/s]	Turb. kin. E [J/kg]	Pressure [pa]	Velocity curl $[s^{-1}]$
NACA0025	2.43	0.0046	-784	3.99
NACA0025 Circular	2.85	0.0206	-397	1.81
NACA0025 Elliptic	2.80	0.0228	-442	1.85

Finally for the vortex reduction comparison, the volumes of fluid around the geometries containing vorticity larger than $1.0026\ s^{-1}$, also called the vortex cores, are plotted for each geometry for comparison in visualisation of the vortices in figures 38 to 40.
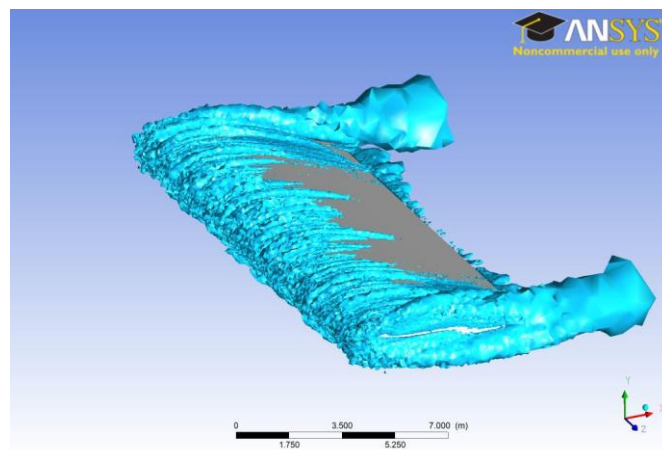
Figure 38: Vortex core region for the NACA0025 geometry.
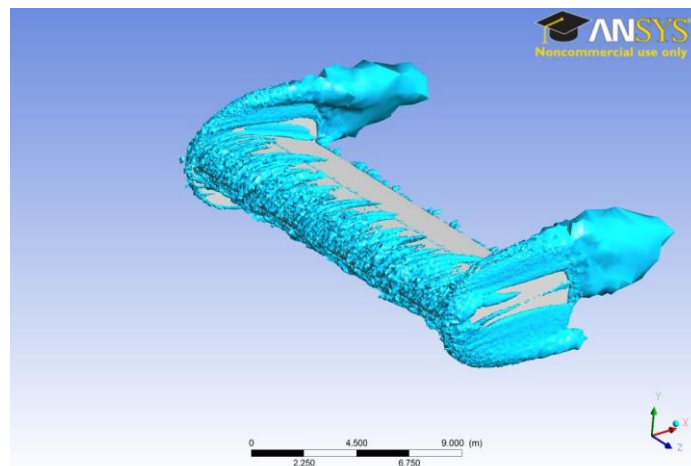
Figure 39: Vortex core region for the NACA0025 geometry with elliptical end plates.
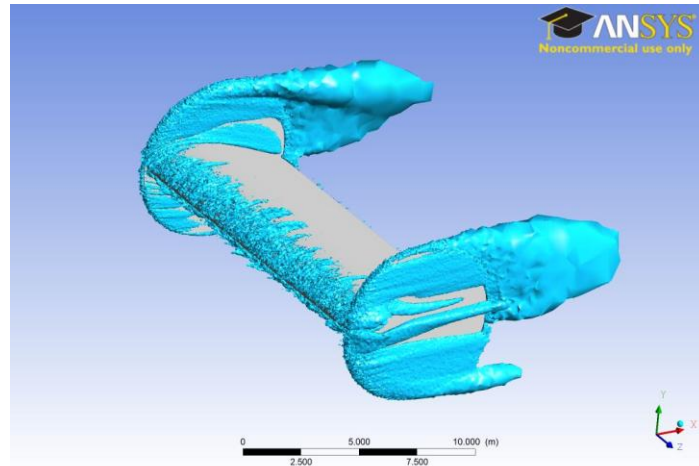
Figure 40: Vortex core region for the NACA0025 geometry with circular end plates.

4.4.4   Pressure profiles on geometries with endplates

The addition of end plates to the NACA0025 profile also had the advantage of creating a less elliptical pressure distribution than the NACA0025 with free tips. This can be shown by plotting the pressure distribution along a number of polylines created over around the hydrofoil as seen in figure 41 and comparing the results of the graphs. The results are shown in figures 42 to 44.
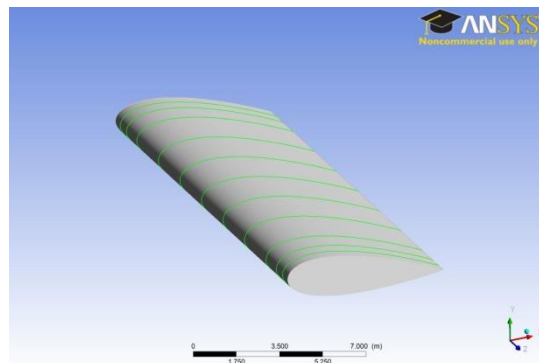
Figure 41: NACA0025 geometry with polylines around the surface it at 1m spacing.

The pressure distributions around the polylines are plotted in a graph for the NACA0025 geometry along with the geometries with the added end plates.
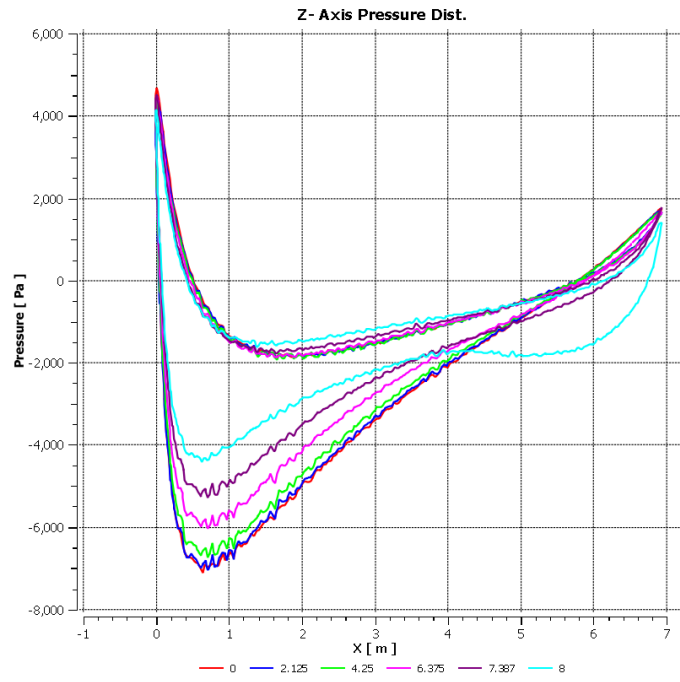
Figure 42: Pressure distributions around polyines for the NACA0025 geometry.
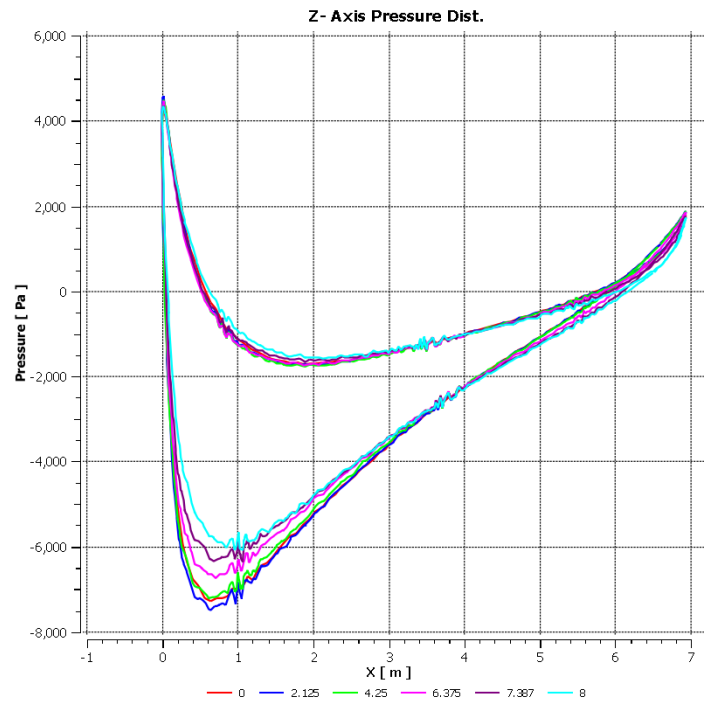
Figure 43: Pressure distributions around polyines for the NACA0025 geometry with elliptical end plates

.
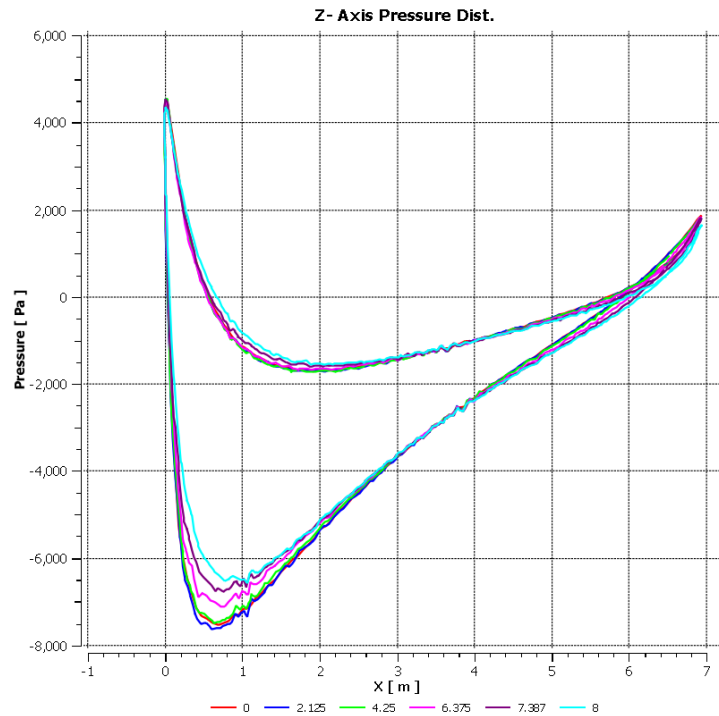
Figure 44: Pressure distributions around polylines for the NACA0025 geometry with circular end plates.

5 Conclusions and discussion

In this chapter the conclusions drawn from the different parts of the project are presented along with a discussion of the feasibility of the hydrofoil as a concept. The chapter also contains some preliminary economical calculations based on the electricity production for a certain operating depth and an evaluation of the CFD studies accuracy. Finally, there are some suggestions on future work.

5.1 Verification

As seen in figure 16 in section 4.4.1 the lift coefficient for the 2D NACA0025 was very consistent with the wind tunnel data. The drag on the other hand does not show the same fit to the experimental curve in figure 17, mainly due to the fact that the data is taken from a laminar flow study and Fluent 6.3 simulates a fully turbulent flow over the foil which creates less drag. It was also noted that the y+ value was too high for the Transition SST k- ω model which operates in y+ less than one, but this criteria is only useful in resolving the transition boundary layer which is not present in the hydrofoil flow case.

The calculated drag coefficients were finally compared to experimental tripped turbulent wind tunnel data which gave good agreement. It is therefore possible to conclude that the methods used in the 2D case are valid for high Reynolds number fully turbulent flows such as the one for the hydrofoil.

The models for the 3D case were verified in the same manner as for the 2D case and the results show reasonable agreement for the lift coefficient (figure 18). Fluent does however under predict the lift

48

from 10 degrees AoA and onward in what looks like a stall curve, but in the operational 8 degree AoA for the hydrofoil the fit is very good. The drag was, as for the 2D case, under predicted throughout which was to be expected due to the reasons previously mentioned. The drag is however considered reasonable for a turbulent flow case. Due to the requirement of y+ being less than 1 for the Transition SST k- ω model, the regular SST k- ω model was selected for the 3D case to reduce the computational cost.

5.2 Mesh independence

The mesh independence test for the 2D case shows that the lift and drag coefficients were not dependant on the grid resolution between 87120 and 154560 nodes. Therefore it was considered accurate enough to use the coarsest mesh in order to save computational time.

The same can be said about the 3D case as for the 2D case that the coefficients do not vary considerably with node numbers between approximately $1 \cdot 10^6$ and $3.5 \cdot 10^6$ and thusly a mesh with 2160656 nodes was chosen for the NACA0025 analysis and the other 3D cases were based on that mesh.

5.3 CFD model accuracy

There are a number of limitations imposed on the project ranging from time, computing power to lack of tidal stream turbulent data which makes the simulations less accurate than optimal. Due to the large scale of the geometries used, especially in the 3D modelling, vast amounts of computing power are needed to fully resolve the flow close to the boundary. These calculations are also highly time- consuming which was out of the scope for this project.

In order to close the RANS equation the turbulence models need accurate input data of k and ω as explained in section 2.1.1. For the SST k- ω model to perform correctly in the near- wall region the y+ value must be in range and the user defined values must be accurate since the ω- transport equation (eq 2.26) is sensitive to these free- stream value of ω. The blending function (eq 2.27) also uses the wall distance to define the zonal solution domains which requires a good y+ value.

However, the inaccuracies of the study can be seen as negligible due to the fact that the purpose of the thesis was to conclude if the concept was plausible and determine the preliminary dimensions of the hydrofoil. For this reason the accuracy of the study should be considered sufficient, but for determining the exact operational characteristics of the hydrofoil, more accurate studies are needed especially using transient time schemes. Also, site- specific turbulence data of k and ω must be collected in order to get accurate solutions from the turbulence models.

5.4 2D study

The conclusions drawn from the 2D study were the base on which geometries were to be analysed using 3D modelling.

As the plots show in section 4.3.1, the Joukowski and the Eppler E838 had the highest lift and lowest drag which was expected due to them having more advanced geometries compared to the NACA0025 and NACA00258-75. The Joukowski and Eppler foils also had the largest moment coefficients which could be a drawback in terms of dynamic loadings on the foil and mooring. The

L/D curves also show superior efficiency for the Eppler and Joukowski at 8 degrees AoA, with the two NACA foils having basically the same L/D properties.

However, the seemingly superior efficiency of the Joukowski and Eppler foils in terms of high lift and low drag did not translate to greatly reduced mooring angles. The difference between the smallest angle from the Joukowski and the largest angle from the NACA0025 was only 5.15 degrees. This was due to the slimmer profiles of the advanced foils not having the same buoyancy as the thicker NACA profiles. Table 4 also shows the low B/L ratio of the foils being 0.1831 for the Joukowski and 0.1483 for the Eppler, which was in conflict with the design criteria of high buoyancy set by Nautricity.

Due to the above reasons and assumed construction complexity, the Eppler E838 was not taken to further investigation despite showing good mooring angles at maximum flow velocity. Instead the Joukowski and NACA0025 were chosen for further analysis due to their simplicity and high buoyancy.

5.5 Marine growth

The results from the roughness study showed that increasing the roughness can have a serious negative effect on the lift as well as increasing the drag. It was however found that the effects of the roughness levelled off after a roughness height of 0.01m which is probably due to the coarseness of the mesh close to the surface.

It can be concluded that if marine growth were to be present on the hydrofoil the efficiency of it would deteriorate although the exact extent is unknown. Wind tunnel data [18] also back up the claims of reduced effectiveness due to roughness.

What needs to be established is if there exists any species of marine growth in the chosen site of operation that can attach itself to the surface of the hydrofoil at maximum flow speeds of approximately 4.5 m/s, as seen in the orange area of figure 45. If marine fouling is shown to be present it will be a factor that must be included in the economic evaluation of the hydrofoil due to regular cleaning and application of anti fouling agents.
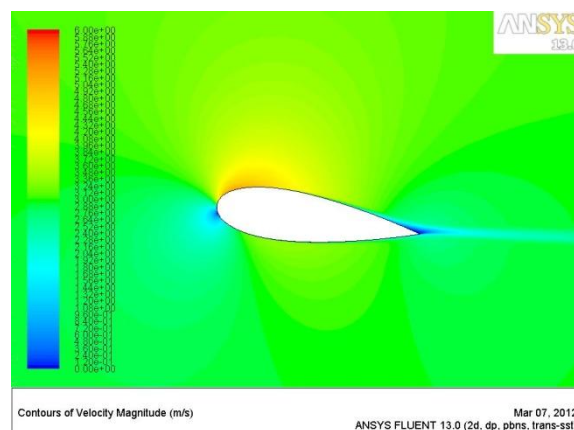

Figure 45: Velocity profile around the NACA0025 foil at 3 m/s flow speed.

5.6   3D study

The results showed that, as expected, the 3D geometry of the Joukowski performed better than the corresponding NACA0025 geometry and that adding end plates to the NACA0025 significantly improved its lift. It can be seen in figure 27 that the circular end plate generates slightly higher lift than the elliptical one. On the other hand, the end plates seem to add more drag to the hydrofoil which is counter intuitive to the arguments in section 2.2.2. This is assumed to be a result of the increased parasitic drag from the plates being larger than the reduced vortex drag. A more detailed discussion on the end plates is presented in the next section.

The high lift devices produced an L/D ratio of about 9 which was the same as for the geometries without flaps. The main difference of the performance with the flaps was that the angle for maximum L/D was shifted to -2 degrees.

When considering the mooring angles that each geometry configuration gives it seems reasonable to add circular end plates to the geometry as this gave a decrease of Φ of 6.75 degrees. The addition of the end plates also significantly reduced the moment coefficients on the structure, probably due to the countering forces from the lower parts of the plates, as seen in figure 29.

For even further mooring angle reduction one could consider adding end plates to the Joukowski geometry and reducing the thickness of the end plates, although this brings along construction issues.

5.7   End plates

The addition of end plates was successful in increasing the lift from the NACA0025 geometry but not in reducing the drag which was the original purpose.

The lift increase is due to the reduction in pressure drop close to the end of the hydrofoil caused by fluid 'bleeding' from the lower to the upper surface due to the pressure gradient. The addition of end plates simply inhibits the flow from the two surfaces to some extent. The removal of pressure reduction near the ends due to end plates can be seen in figures 42 to 44 where the spaces between the lines in figure 42 indicates that there is less pressure difference between the top and bottom of the hydrofoil. The pressure profiles for the geometry with elliptical end plates are closer together which indicates greater pressure difference (fig 43), hence more lift, and the circular plated geometry displays even more pressure difference (fig 44). Hence the circular plate shows the best performance.

Section 4.4.3 shows the end plate's ability to reduce the induced drag. Unfortunately, there was no way to separate the force caused by the parasitic drag from the force caused by the induced drag. Even though the end plates reduce the trailing vortices it must be assumed that they add more parasitic drag since the overall drag curves are larger than for the plain NACA0025. A way of reducing the parasitic drag would be to reduce the thickness to thinner than 0.1m which was used due to construction considerations. Also, one could consider smoothening the edges of the geometry for further drag reduction.

 The reduction of the trailing vortices can be seen in figures 38 to 40 where the vortices are reduced and moved up on to the top of the end plates. Figures 53 to 55 in Appendix C show that the turbulent

kinetic energy is increased with the size of the end plates which may be a result of the trailing vortex being dissipated to turbulence, and possibly the plates themselves causing turbulence.

5.8   High lift devices

The study of the high two geometries with flaps showed that there was no net gain in adding a plain flap to the geometry since the drag increased proportionally to the lift.

The major difference achieved in performance by adding the flap was that the maximum efficiency AoA was shifted to -2 degrees which would cause problems when the hydrofoil is turned further downward in slower flow velocities. This may cause instabilities and unwanted strain on the mooring system.

Due to the reasons mentioned, adding a trailing edge plain flap was not considered to benefit the buoyant hydrofoil design.

5.9   Feasibility and economic considerations

The CFD study shows that the concept of a buoyant hydrofoil as a lifting device for the CoRMaT is theoretically possible in terms of lift generated, but one must take several economical and stability factors into consideration.

One obvious factor is the cost of manufacturing a hydrofoil as compared to using commercially available off the shelf buoys. The study conducted by the student team MORE at Strathclyde University (section 1.4.3) showed that a spherical buoy with a diameter of 5m gave a 40 degree mooring angle, although commercial cylindrical buoys can be expected to give slightly larger angles.

Using Excel sheets written by the MORE team it was possible to get an estimate of the performance of a cylindrical buoy station keeping device with the same volume and density as the investigated hydrofoil. A case was set up in a theoretical site of a water depth of 100m and a mooring cable to the turbine of 65m length where the performances of the buoy and the hydrofoil were compared. A 7th power law tidal velocity profile (2.3.2) was assumed for the stream and the semi- diurnal and bi-monthly velocity variations (2.3) were also considered. Using the equation for power output for MCT's (2.4.1), drag equation (2.2.2), the buoyancy equation (2.2.4) and the relationship of L/D and Φ it was possible to get the annual energy generation and annual income for the two cases. The values and assumptions fed in to the Excel sheet are shown in table 7:

Table 7: Values imputed to the Excel sheet to get the average energy production. Some values are assumed constant for ease of calculation.

Hydrofoil		Buoy	
Chord	7m	Diameter	3m
Width	17m	Height	3m
Volume	20.22 m^3	Volume	21.2m^3
Density	500 kg/m^3	Density	500 kg/m^3
Total drag (spring) (constant)	292375 N	Total drag (spring) (constant)	2395000 N
Total L and B (spring) (constant)	360827 N	Total L and B (spring) (constant)	109200 N
Mooring angle (spring) (constant)	39.01 degrees	Mooring angle (spring) (constant)	65.5 degrees
Operating height (spring) (constant)	50 m	Operating height (spring) (constant)	27 m
Maximum spring tide velocity at 50m	2.72m/s	Maximum spring tide velocity at 27m	2.48m/s
Total drag (neap) (constant)	76567 N	Total drag (neap) (constant)	73000 N
Total L and B (neap) (constant)	180514 N	Total L and B (neap) (constant)	109200 N
Mooring angle (neap) (constant)	22.98 degrees	Mooring angle (neap) (constant)	33.8 degrees
Operating height (neap) (constant)	60 m	Operating height (neap) (constant)	54m
Maximum neap tide velocity at 60m	1.39m/s	Maximum neap tide velocity at 54m	1.37m/s
Semi- diurnal period	12.5h	Semi- diurnal period	12.5h
Bi- monthly period	14 days	Bi- monthly period	14 days
Cut in velocity	1m/s	Cut in velocity	1m/s
Rated velocity	2.5m/s	Rated velocity	2.5m/s
Rotor diameter	10m	Rotor diameter	10m
Rated power	250kW	Rated power	250kW

The result from the power generation calculation showed that the annual energy production for the turbine specifications in table 7 was 573.5 MWh using a hydrofoil configuration and 471.1 Mwh for a configuration using a buoy. This shows that using a hydrofoil increases the turbines production by 21.8% for the case above. If one assumes a wholesale electricity price of £40/Mwh and 5 Renewable energy obligations each worth £50/Mwh which gives a total income per Mwh of £209/Mwh [10], using a hydrofoil for the CoRMaT yields £29,786/year extra income. If the extra cost of the hydrofoil manufacture was known one could calculate the 'break even' time required, but this is considered out of the scope of this thesis.

Another major issue yet to be dealt with is the stability of the hydrofoil in the tidal stream. Since the generated lift is sensitive for changes in AoA the device may become unstable if perturbed by external forces such as surface waves. This phenomenon must be investigated thoroughly using numerical simulations and scale model testing.

5.10 Future work

As mentioned in the previous section, there are still many unanswered questions regarding the hydrofoil. The main topic in the sense of CFD investigations is to analyse the behaviour of the hydrofoil in a transient time analysis to determine the behaviour during the full tidal cycle. The stability of the hydrofoil is also an issue that has to be investigated both by numerical methods and scale model testing.

Another task would involve redoing steady- state analysis for the NACA0025 with circular end plates with very fine mesh resolution near the surface to fully resolve the boundary layer for greater accuracy of the final structure. Also, a more detailed investigation into the turbulent behaviour of tidal streams should be conducted and the results integrated into the CFD simulation.

6   References

 [1] **The Scottish government.** (2009) "Climate Change Delivery Plan: Meeting Scotland's Statutory Climate Change Targets"

[2] **Marine turbines web site.** (2012) http://www.marineturbines.com/Tidal-Energy

[3]**Sea Generation Ldt. website**. (2012) http://www.seageneration.co.uk/

[4] **Grant, A.** "Exploitation of tidal currents", Lecture material from Renewable energy systems course MCT.pdf

[5] **Fraenkel, P. L.** (2006) "Tidal current energy technologies", Marine current turbines Ldt,

[6] **Strathclyde University SEN Communications.** (2010) "Enterprise matters issue 22", Strathclyde University

[7] **Grant, A**. "Tidal energy conversion", Lecture material from Renewable energy systems course

[8] **Clarke, J and Connor, G and Grant, A and Johnstone, C and Ordonez- Sanches, S. "**A Contra-rotating Marine Current Turbine on a Flexible Mooring: Development of a Scaled Prototype**",** Energy Systems Research Unit, Dept. of Mechanical Engineering, University of Strathclyde

[9] **Clarke, J and Connor, G and Grant, A and Johnstone, C.** (2006) **"**Design and testing of a contra-rotating tidal current turbine**",** Energy Systems Research Unit, Dept. of Mechanical Engineering, University of Strathclyde

[10]**MORE Student group web page** (2012) http://www.esru.strath.ac.uk/EandE/Web_sites/11-12/MORE/more_info/team.html

[11] **Versteeg, H and Malalasekera, W.** (2007) "An Introduction to Computational Fluid Dynamics: The Finite Volume Method (2nd Edition)", Pearson

[12] **Orszag, S.A.** (1970) "Analytical theories of turbulence", Journal of Fluid Mechanics / Volume 41 / Issue 02 / April 1970 , pp 363-386

[13] **Flood Manager web page.** (2012) "Lecture material", http://daad.wb.tu-harburg.de/fileadmin/BackUsersResources/Flood_Probability/2D/Steffi-2D/pdf/Reynolds_average_Navier-Stokes_equation.pdf

[14] **Fluent 6.3 Manual** "*FLUENT 6.3 manual chapter 12: Modelling Turbulence*"

[15] **Barltrop, N. and Varyani, K.S. and Grant, A.D. and Clelland, D. and Pham, X.P.** (2007) "Investigation into wave-current interactions in marine current turbines", Department of Mechanical and Aerospace Engineering

[16] **Norris, J.V. and Droniou, E.** (2007) "Update on EMEC activities, resource description, and characterisation of wave-induced velocities in a tidal flow" , Proceedings of the 7th European Wave and Tidal Energy Conference, Porto, Portugal.

[17] **De Chant, L.J.** (2005) " The venerable 1/7th power law turbulent velocity profile: a classical nonlinear boundary value problem solution and its relationship to stochastic processes " , Applied Mathematics and Computation, Vol. 161, pp. 463-474.

[18] **Abbot, I.H and Von Doenhof, A.E** (1960) "Theory of wing sections", Dover Publications Inc

[19] **UIUC Applied Aerodynamics Group web page** (2012) "UIUC Airfoil coordinates database", http://www.ae.illinois.edu/m-selig/ads/coord_database.html

[20] **McCroskey, W.J** (1987) "A Critical Assessment of Wind Tunnel Results for the NACA0012 Airfoil", NASA Technical Memorandum, Aeroflightdynamics Directorate, U.S. Army Aviation Research and Technology Activity, Ames Research Center, Moffett Field, California

Figure references

1: **Lecture material** from ME504 Renewable energy systems at Strathclyde University

2: **Wikipedia commons**
http://commons.wikimedia.org/wiki/File:SeaGen,_Strangford,_June_2011_(02).JPG

3, 4: Nautricity web page http://www.nautricity.com/cormat/

6: **Flood manager web page**, http://daad.wb.tu-harburg.de/fileadmin/BackUsersResources/Flood_Probability/2D/Steffi-2D/pdf/Reynolds_average_Navier-Stokes_equation.pdf

7 Appendix A

Hydrofoil profiles
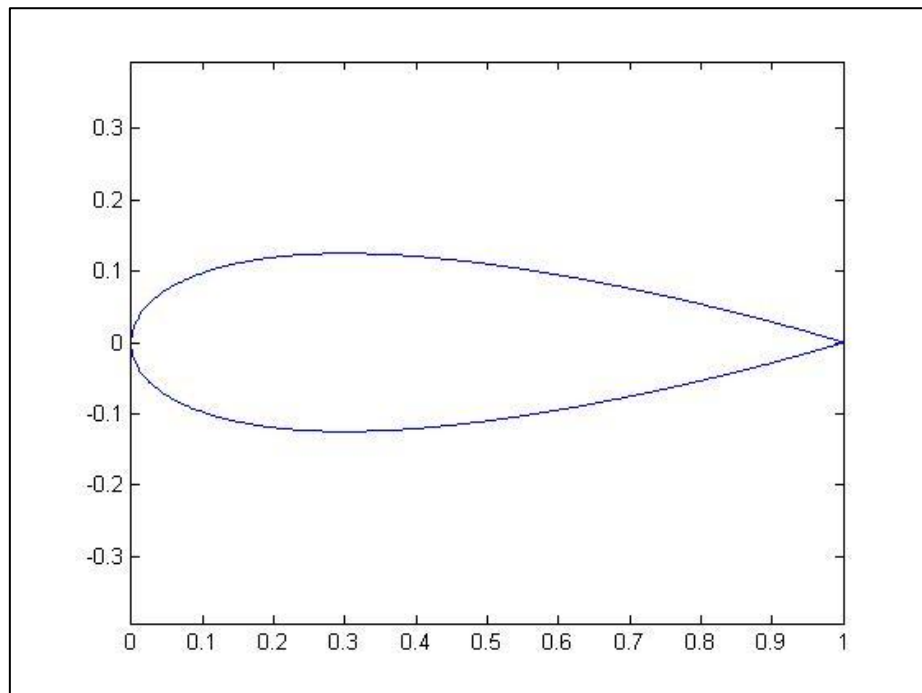
Figure 46: NACA0025
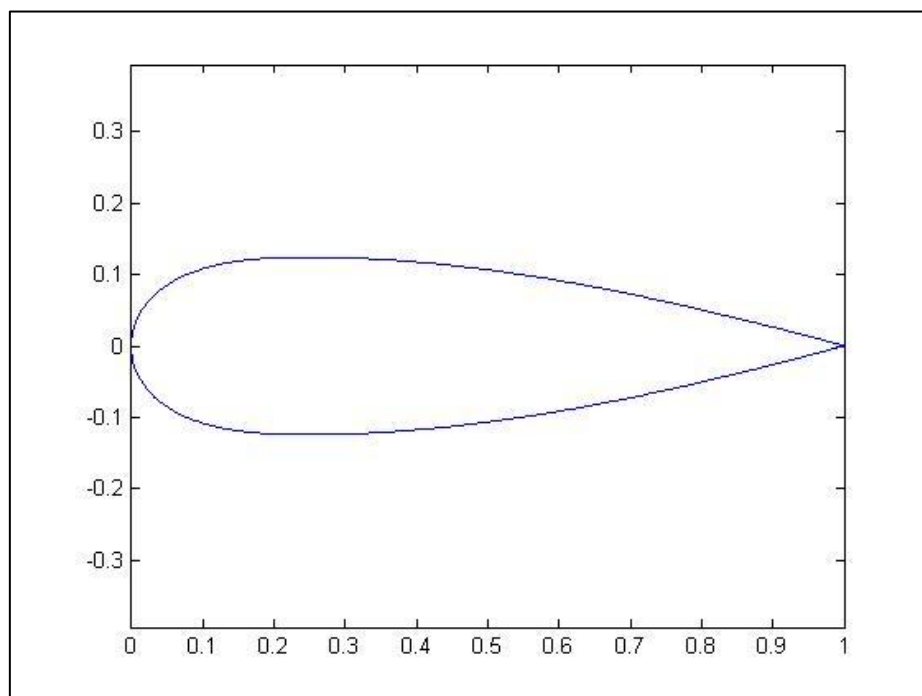
Figure 47: NACA0025-72
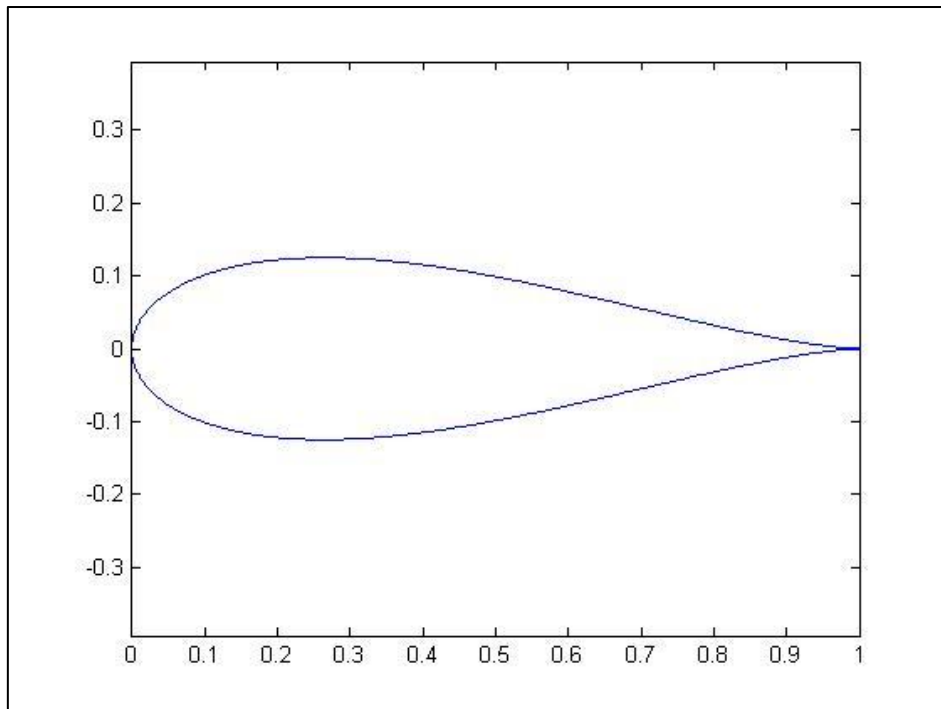
Figure 48: Joukowski
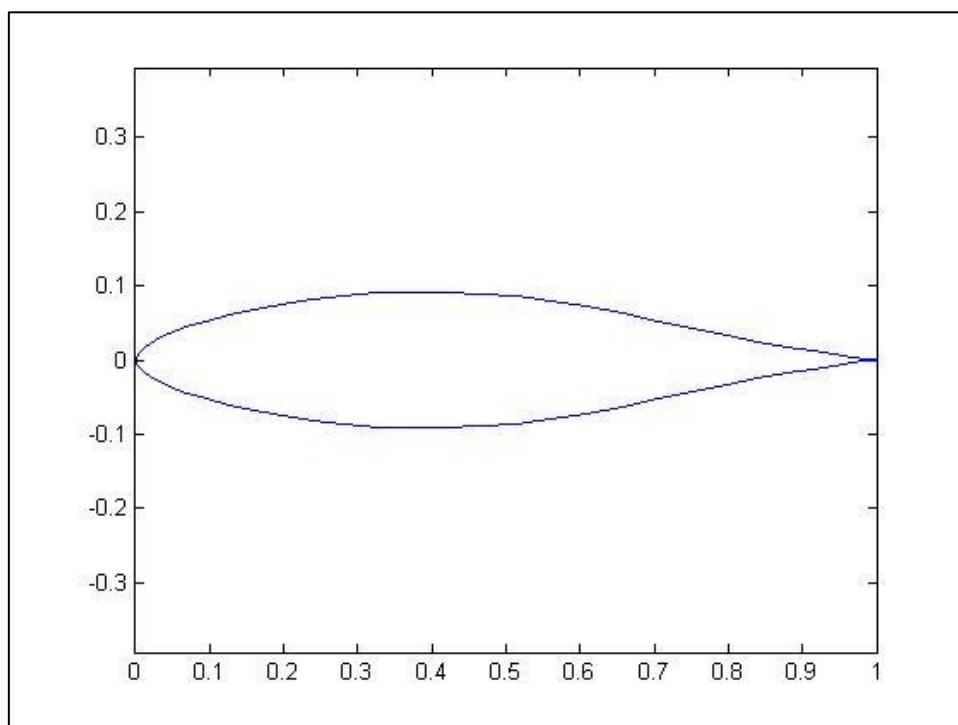
Figure 49: Eppler E838

57

8   Appendix B

Matlab script

```
clear all
clc

%2D RESULTS
%Eppler E838
d=456.58*17;
l=28270*17;
length=7;
width=17;
rho_float=500;
Aside=0.1162*length;
volume=Aside*width;
mass=volume*rho_float;
weight=mass*9.82;

dt=0.5*1025*3^2*0.85*78;
b=(2*9.82*mass*1025*volume)/(mass+1025*volume);

disp('Eppler results')
percentage1=b/l
theta1=atand((d+dt)/(b-weight+l))

%NACA0025
d=503*17;
l=22678*17;
length=7;
width=17;
rho_float=500;
Aside=0.16993*length;
volume=Aside*width;
mass=volume*rho_float;
weight=mass*9.82;

dt=0.5*1000*3^2*0.85*78;
b=(2*9.82*mass*1025*volume)/(mass+1025*volume);

disp('NACA0025 results')
percentage2=b/l
theta2=atand((d+dt)/(b-weight+l))

%Jaukowski
d=525.29*17;
l=30080*17;
length=7;
width=17;
rho_float=500;
Aside=0.1526*length;
volume=Aside*width;
mass=volume*rho_float;
weight=mass*9.82;

dt=0.5*1000*3^2*0.85*78;
b=(2*9.82*mass*1025*volume)/(mass+1025*volume);
```

```
disp('Jaukowski results')
percentage3=b/l
theta3=atand((d+dt)/(b-weight+l))

%NACA0025-72
d=509.8*17;
l=24189*17;
length=7;
width=17;
rho_float=500;
Aside=0.1698*length;
volume=Aside*width;
mass=volume*rho_float;
weight=mass*9.82;

dt=0.5*1025*3^2*0.85*78;
b=(2*9.82*mass*1025*volume)/(mass+1025*volume);

disp('NACA0025-72')
percentage4=b/l
theta4=atand((d+dt)/(b-weight+l))

%3D RESULTS

%NACA0025 3D
d=24880;
l=223663;
length=7;
width=17;
rho_float=500;
Aside=0.16993*length;
volume=Aside*width;
mass=volume*rho_float;
weight=mass*9.82;

dt=0.5*1025*3^2*0.85*78;
b=(2*9.82*mass*1025*volume)/(mass+1025*volume);

disp('NACA0025 3D')
percentage6=b/l
theta6=atand((d+dt)/(b-weight+l))


%NACA0025 Elliptic end plate
d=30700;
l=279938;
length=7;
width=17;
rho_float=500;
rho_w=700;
Aside=0.16993*length;
volume=Aside*width;
massf=volume*rho_float;
massw=rho_w*2.8863;
weight=(massf+2*massw)*9.82;
```

```matlab
dt=0.5*1025*3^2*0.85*78;
b=(2*9.82*mass*1025*volume)/(mass+1025*volume);
bw=(2*9.82*massw*1025*2.8863)/(massw+1025*2.8863);

disp('NACA0025 3D ellipse')
percentage6=(b+2*bw)/l
theta7=atand((d+dt)/(b+2*bw-weight+l))

%NACA0025 Circular end plate
d=32194;
l=296172;
length=7;
width=17;
rho_float=500;
rho_w=700;
Aside=0.16993*length;
volume=Aside*width;
massf=volume*rho_float;
massw=rho_w*3.8484;
weight=(massf+2*massw)*9.82;

dt=0.5*1025*3^2*0.85*78;
b=(2*9.82*mass*1025*volume)/(mass+1025*volume);
bw=(2*9.82*massw*1025*3.8484)/(massw+1025*3.8484);

disp('NACA0025 3D circle')
percentage7=(b+2*bw)/l
theta7=atand((d+dt)/(b+2*bw-weight+l))
```

9 Appendix C

Images of trailing edge vortices
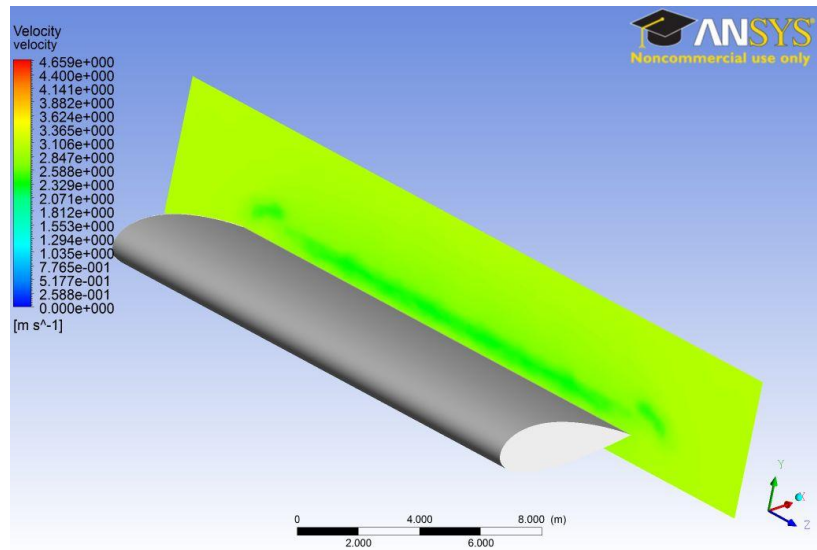
Figure 50: Velocity distribution plotted 1m behind the NACA0025 profile.
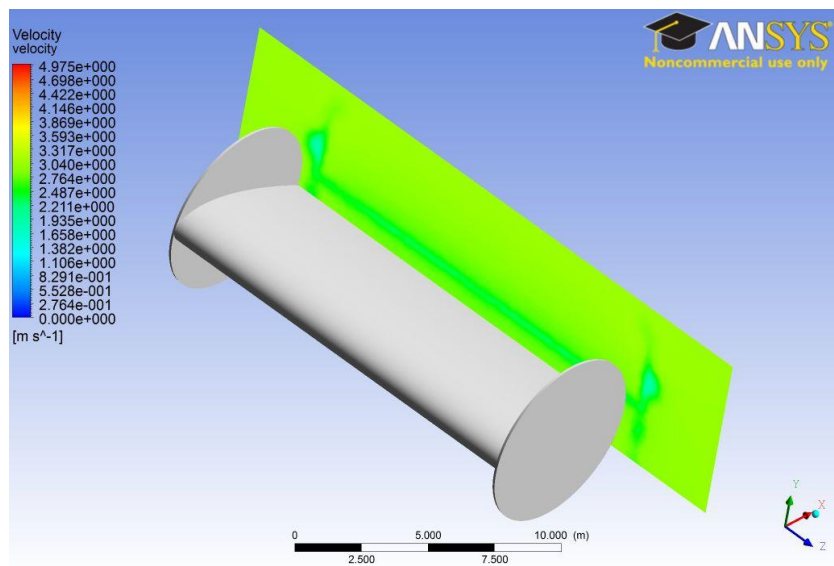
Figure 51: Velocity distribution plotted 1m behind the NACA0025 profile with circular end plate.

Figure 52: Velocity distribution plotted 1m behind the NACA0025 profile with elliptical end plate.

Figure 53: Turbulent kinetic energy distribution plotted 1m behind the NACA0025 profile.
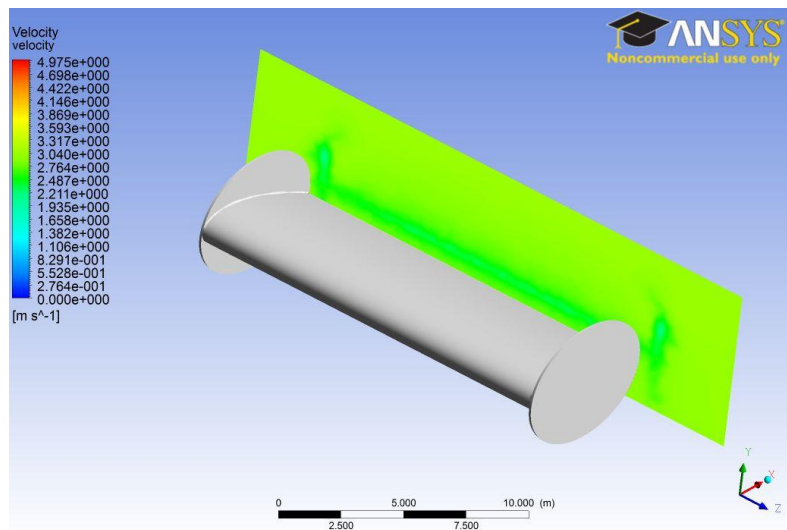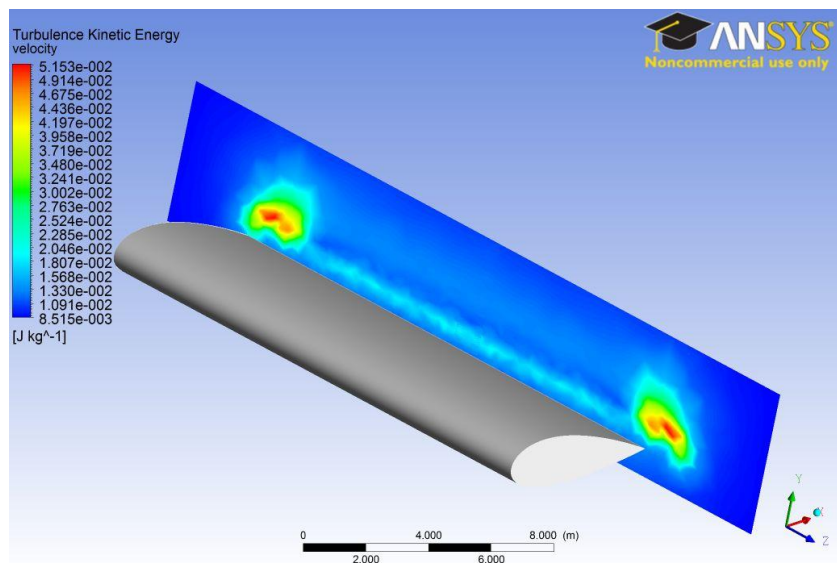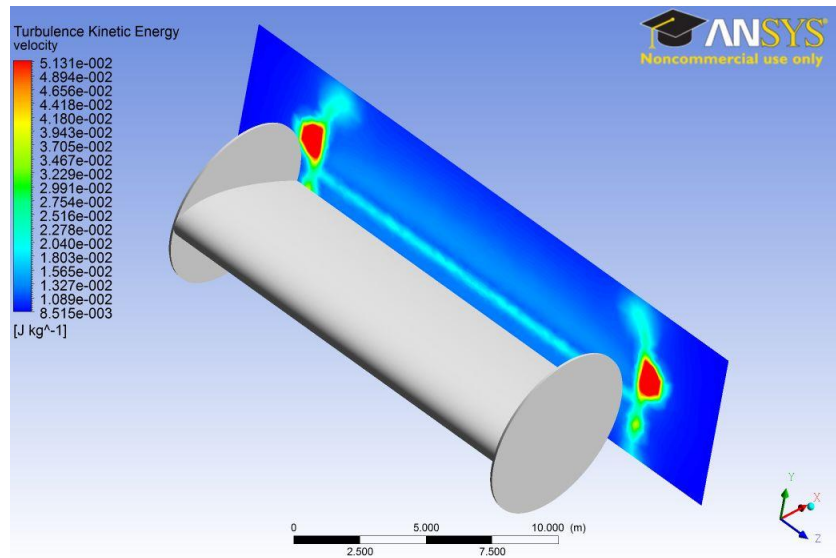
62

Figure 54: Turbulent kinetic energy distribution plotted 1m behind the NACA0025 with circular end plate.
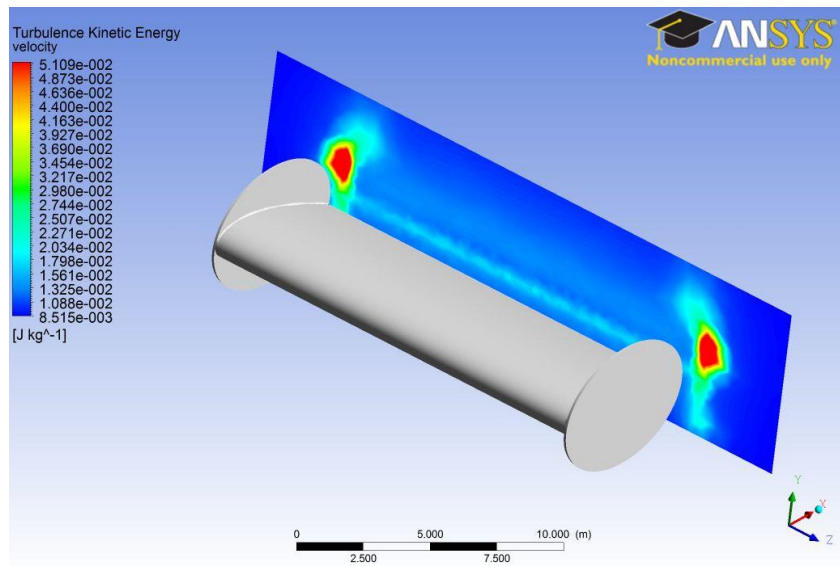
Figure 55: Turbulent kinetic energy distribution plotted 1m behind the NACA0025 with elliptical end plate.

10 Appendix D

2D Numerical data

Table 8: Numerical values from the 2D NACA0025 run.

AoA [degrees]	CD	CL	CM	L [N]	D [N]	M [Nm]
0	0.011	0.0001	0	3	370	5
2	0.0117	0.1596	0.0281	5155	377	-2671
4	00.123	0.3353	0.0367	10828	400	-4534
6	0.0136	0.5202	0.1041	16797	440	-5849
8	0.0155	0.7023	0.1442	22678	503	-7085
10	0.0184	0.8738	0.1810	28215	594	-8431

Table 9: Numerical values from the 2D NACA0025-72 run.

AoA [degrees]	CD	CL	CM	L [N]	D [N]	M [Nm]
0	0.01147	0	0	0	370	0
2	0.01171	0.238	0.0351	5757	378	-2123
4	0.01246	0.4757	0.0760	11903	402	-3642
6	0.01379	0.7082	0.1184	18129	445	-4946
8	0.01597	0.9316	0.1594	24189	509	-6284
10	0.01866	1.1366	0.1969	29873	602	-7769

Table 10: Numerical values from the 2D Joukowski run.

AoA [degrees]	CD	CL	CM	L [N]	D [N]	M [Nm]
0	0.0109	0	0	0	354	0
2	0.0112	0.238	0.0626	7710	364	662
4	0.01224	0.4758	0.1245	15364	395	1263
6	0.01387	0.7082	0.1866	22869	448	1713
8	0.01626	0.9316	0.2410	30080	525	1917
10	0.01972	1.1366	0.2920	36699	636	1780

Table 11: Numerical values from the 2D Eppler E838 run.

AoA [degrees]	CD	CL	CM	L [N]	D [N]	M [Nm]
0	0.0091	0	0	0	294	-33
2	0.0094	0.22	0.0594	7232	303	801
4	0.0102	0.446	0.1185	14428	331	1549
6	0.01179	0.6651	0.1750	21475	380	2102
8	0.01414	0.8736	0.2280	28207	456	2304
10	0.01764	1.06	0.2736	34259	569	1887

3D numerical data

Table 12: Numerical values for the 3D NACA0025 run. L, D and M have been multiplied by 2 due to symmetry.

AoA [degrees]	CD	CL	CM	L [N]	D [N]	M [Nm]
0	0.0208	0.0017	0.0046	987	11470	4700
2	0.0224	0.1023	0.0901	56188	12336	90246
4	0.0270	0.2025	0.1744	111194	14842	174574
6	0.0347	0.3050	0.2644	167460	19062	264724
8	0.0453	0.4074	0.3545	223663	24880	354921
10	0.0587	0.5079	0.4426	278828	32262	443018
12	0.0754	0.6104	0.5365	335056	41432	537066
14	0.0949	0.7092	0.6276	389313	52136	628190

Table 13: Numerical values for the 3D Joukowski run. L, D and M have been multiplied by 2 due to symmetry.

AoA [degrees]	CD	CL	CM	L [N]	D [N]	M [Nm]
0	0.0210	0	0.0005	126	11527	530
2	0.0228	0.1118	0.1090	61410	12546	109156
4	0.0282	0.2229	0.2172	122380	15491	217494
6	0.0370	0.3338	0.3255	183220	20338	325856
8	0.0495	0.4475	0.4396	245630	27214	140094
10	0.0658	0.5615	0.5567	308248	36140	278629
12	0.0860	0.6769	0.6712	371560	47224	678902
14	0.1100	0.7924	0.8026	434986	60428	803408

Table 14: Numerical values for the 3D NACA0025 Elliptical run. L, D and M have been multiplied by 2 due to symmetry.

AoA [degrees]	CD	CL	CM	L [N]	D [N]	M [Nm]
0	0.0291	0.0018	0.0009	-1024	15947	-3812
2	0.0307	0.1274	0.0306	69944	16878	117588
4	0.0357	0.2555	0.0614	140242	19618	236282
6	0.0442	0.3839	0.0927	210744	24270	356358
8	0.0559	0.5106	0.1229	279938	30682	472320
10	0.0707	0.6336	0.1521	347775	38848	584704
12	0.0886	0.7560	0.1811	414972	48662	695962
14	0.1092	0.8739	0.2085	479700	59976	801262

Table 15: Numerical values for the 3D NACA0025 Circular run. L, D and M have been multiplied by 2 due to symmetry.

AoA [degrees]	CD	CL	CM	L [N]	D [N]	M [Nm]
0	0.0320	0	0	0	17606	190
2	0.0337	0.1373	0.0340	75400	18532	130752
4	0.0387	0.2728	0.0670	149764	21278	257472
6	0.0470	0.4063	0.0990	223022	25818	380580
8	0.0586	0.5395	0.1311	296172	32194	503864
10	0.0735	0.6721	0.1630	368924	40338	626574
12	0.0917	0.8053	0.1946	440964	50338	747858
14	0.1128	0.9321	0.2252	511534	61918	865604

Table 16: Numerical values for the 3D Joukowski Flap run. L, D and M have been multiplied by 2 due to symmetry.

AoA [degrees]	CD	CL	CM	L [N]	D [N]	M [Nm]
-8	0.0258	0.1104	0.1779	60634	14202	683734
-6	0.0300	0.2242	0.2089	123074	16506	802762
-4	0.0378	0.3357	0.2380	184290	20770	914682
-2	0.0491	0.4475	0.2670	245628	26976	1025916
0	0.0641	0.5593	0.2962	307008	35216	113842
2	0.0825	0.6709	0.3256	368280	45326	1251384
4	0.1044	0.7825	0.3552	429536	57332	1364942
6	0.1297	0.8940	0.3850	490758	71218	1479508
8	0.1584	1.0050	0.4150	551662	86970	1594646
10	0.1900	1.1135	0.4441	611216	104294	1706576
12	0.2236	1.2164	0.4710	667696	122742	1809984
14	0.2596	1.3149	0.4967	721744	142502	1908514

Table 17: Numerical values for the 3D NACA0025 Flap run. L, D and M have been multiplied by 2 due to symmetry.

AoA [degrees]	CD	CL	CM	L [N]	D [N]	M [Nm]
-8	0.0285	0.1255	0.1933	68890	15693	742952
-6	0.0326	0.2300	0.2187	126286	17930	840382
-4	0.0399	0.3341	0.2440	183406	21946	937830
-2	0.0509	0.4400	0.2704	241544	27966	1039080
0	0.0649	0.5434	0.2956	298310	35650	1136052
2	0.0823	0.6495	0.3224	356506	45174	1239100
4	0.1019	0.7511	0.3469	412316	55956	1332952
6	0.1247	.08538	0.3723	468682	68456	1430642
8	0.1501	0.9542	0.3971	523780	82434	1525874
10	0.1782	1.0516	0.4211	577257	97840	1618038
12	0.2103	1.1521	0.4474	632390	115446	1719082
14	0.2447	1.2490	0.4726	685560	134330	1816176